HUBBLE SPACE TELESCOPE ACS MULTIBAND CORONAGRAPHIC IMAGING OF THE DEBRIS DISK AROUND β PICTORIS[1]

D. A. Golimowski,[2] D. R. Ardila,[3] J. E. Krist,[4] M. Clampin,[5] H. C. Ford,[2] G. D. Illingworth,[6] F. Bartko,[7]
N. Benítez,[8] J. P. Blakeslee,[9] R. J. Bouwens,[6] L. D. Bradley,[2] T. J. Broadhurst,[10] R. A. Brown,[11]
C. J. Burrows,[12] E. S. Cheng,[13] N. J. G. Cross,[14] R. Demarco,[2] P. D. Feldman,[2] M. Franx,[15]
T. Goto,[16] C. Gronwall,[17] G. F. Hartig,[11] B. P. Holden,[6] N. L. Homeier,[2] L. Infante,[18]
M. J. Jee,[2] R. A. Kimble,[5] M. P. Lesser,[19] A. R. Martel,[2] S. Mei,[2] F. Menanteau,[2]
G. R. Meurer,[2] G. K. Miley,[15] V. Motta,[18] M. Postman,[11] P. Rosati,[20]
M. Sirianni,[11] W. B. Sparks,[11] H. D. Tran,[21] Z. I. Tsvetanov,[2]
R. L. White,[11] W. Zheng,[2] AND A. W. Zirm[2]

ABSTRACT

We present F435W (*B*), F606W (broad *V*), and F814W (broad *I*) coronagraphic images of the debris disk around β Pictoris obtained with the *Hubble Space Telescope*'s Advanced Camera for Surveys. These images provide the most photometrically accurate and morphologically detailed views of the disk between 30 and 300 AU from the star ever recorded in scattered light. We confirm that the previously reported warp in the inner disk is a distinct secondary disk inclined by ~5° from the main disk. The projected spine of the secondary disk coincides with the isophotal inflections, or "butterfly asymmetry," previously seen at large distances from the star. We also confirm that the opposing extensions of the main disk have different position angles, but we find that this "wing-tilt asymmetry" is centered on the star rather than offset from it, as previously reported. The main disk's northeast extension is linear from 80 to 250 AU, but the southwest extension is distinctly bowed with an amplitude of ~1 AU over the same region. Both extensions of the secondary disk appear linear, but not collinear, from 80 to 150 AU. Within ~120 AU of the star, the main disk is ~50% thinner than previously reported. The surface brightness profiles along the spine of the main disk are fitted with four distinct radial power laws between 40 and 250 AU, while those of the secondary disk between 80 and 150 AU are fitted with single power laws. These discrepancies suggest that the two disks have different grain compositions or size distributions. The F606W/F435W and F814W/F435W flux ratios of the composite disk are nonuniform and asymmetric about both projected axes of the disk. The disk's northwest region appears 20%–30% redder than its southeast region, which is inconsistent with the notion that forward scattering from the nearer northwest side of the disk should diminish with increasing wavelength. Within ~120 AU, the $m_{F435W} - m_{F606W}$ and $m_{F435W} - m_{F814W}$ colors along the spine of the main disk are ~10% and ~20% redder, respectively, than those of β Pic. These colors increasingly redden beyond ~120 AU, becoming 25% and 40% redder, respectively, than the star at 250 AU. These measurements overrule previous determinations that the disk is composed of neutrally scattering grains. The change in color gradient at ~120 AU nearly coincides with the prominent inflection in the surface brightness profile at ~115 AU and the expected water-ice sublimation boundary. We compare the observed red colors within ~120 AU with the simulated colors of nonicy grains having a radial number density $\propto r^{-3}$ and different compositions, porosities, and minimum grain sizes. The observed colors are consistent with those of compact or moderately porous grains of astronomical silicate and/or graphite with sizes ≳0.15–0.20 μm, but the colors are inconsistent with the blue colors expected from grains with porosities ≳90%. The increasingly red colors beyond the ice sublimation zone may indicate the condensation of icy mantles on the refractory grains, or they may reflect an increasing minimum grain size caused by the cessation of cometary activity.

Key words: circumstellar matter — planetary systems: formation — planetary systems: protoplanetary disks — stars: individual (β Pictoris)

Online material: tar file

[2] Department of Physics and Astronomy, The Johns Hopkins University, 3400 North Charles Street, Baltimore, MD 21218-2686.
[3] Spitzer Science Center, Infrared Processing and Analysis Center, MS 220-6, California Institute of Technology, Pasadena, CA 91125.
[4] Jet Propulsion Laboratory, 4800 Oak Grove Drive, MS 183-900, Pasadena, CA 91109.
[5] NASA Goddard Space Flight Center, Code 681, Greenbelt, MD 20771.
[6] Lick Observatory, University of California at Santa Cruz, 1156 High Street, Santa Cruz, CA 95064.
[7] Bartko Science and Technology, 14520 Akron Street, Brighton, CO 80602.
[8] Instituto de Astrofísica de Andalucía, CSIC, Camino Bajo de Huétor, 24, Granada 18008, Spain.
[9] Department of Physics and Astronomy, Washington State University, Pullman, WA 99164.
[10] School of Physics and Astronomy, Tel Aviv University, Tel Aviv 69978, Israel.
[11] Space Telescope Science Institute, 3700 San Martin Drive, Baltimore, MD 21218.
[12] Metajiva, 12320 Scenic Drive, Edmonds, WA 98026.
[13] Conceptual Analytics, LLC, 8209 Woburn Abbey Road, Glenn Dale, MD 20769.

1. INTRODUCTION

Since the initial discoveries of cool (∼100 K) dust around nearby stars by the *Infrared Astronomical Satellite* (Aumann 1985), β Pictoris has been the foremost example of a young, main-sequence star with a resolved circumstellar disk of dust. The disk likely comprises the debris from disintegrating bodies in a nascent planetary system rather than primordial dust from the dissipating protostellar nebula (Backman & Paresce 1993; Artymowicz 1997; Lagrange et al. 2000; Zuckerman 2001). Spectroscopic evidence of multitudinous star-grazing comets (Lagrange-Henri et al. 1988; Beust et al. 1990; Vidal-Madjar et al. 1994 and references therein) has motivated models of the disk as an admixture of gas and dust from colliding and evaporating comets located within a few tens of AU from β Pic (Lecavelier des Etangs et al. 1996; Beust & Morbidelli 1996; Thébault et al. 2003). The cometary origin of the dust is supported by the detection of broad, 10 μm silicate emission such as that observed in the spectra of comets Halley, Kohoutek, and others (Telesco & Knacke 1991; Knacke et al. 1993; Aitken et al. 1993; Weinberger et al. 2003; Okamoto et al. 2004).

Ground-based, coronagraphic images of β Pic reveal an asymmetric, flared disk extending at least 1800 AU from the star and viewed nearly edge-on (Smith & Terrile 1984; Paresce & Burrows 1987; Golimowski et al. 1993; Kalas & Jewitt 1995; Mouillet et al. 1997a; Larwood & Kalas 2001). High-resolution *Hubble Space Telescope* (*HST*) and adaptive optics images show that the inner part of the disk (∼20–100 AU from β Pic) is warped in a manner consistent with the presence of a secondary disk that is inclined by ∼5° from the main disk and perhaps sustained by a massive planet in a similarly inclined eccentric orbit (Burrows et al. 1995; Mouillet et al. 1997b; Heap et al. 2000; Augereau et al. 2001). *HST* and ground-based images also reveal concentrations of dust along the northeast extension of the disk about 500–800 AU from the star that have been interpreted as an asymmetric system of rings formed, along with other asymmetries in the disk, after a close encounter with a passing star (Kalas et al. 2000, 2001; Larwood & Kalas 2001). Spatially resolved mid-infrared images show an asymmetric inner disk having depleted dust within 40 AU of β Pic (Lagage & Pantin 1994; Pantin et al. 1997) and oblique clumps of emission 20–80 AU from the star (Wahhaj et al. 2003; Weinberger et al. 2003; Telesco et al. 2005). These features suggest the presence of noncoplanar dust rings whose locations conform to the mean-motion resonances of a putative planetary system.

Constraints on the sizes of the dust grains observed in scattered light have been based on multiband (*BVRI*) imaging studies of the disk in both unpolarized (Paresce & Burrows 1987; Lecavelier des Etangs et al. 1993) and polarized (Gledhill et al. 1991; Wolstencroft et al. 1995) light. The unpolarized images indicate that the disk is colorless (within uncertainties of 20%–30%) at distances 100–300 AU from β Pic, although its *B*-band

brightness may be suppressed at 50 AU from the star.[22] This neutral scattering by the disk has been customarily viewed as evidence that the dust grains are much larger than the wavelengths of the scattered light (≫1 μm). However, Chini et al. (1991) noted that the *B*-, *V*-, and *I*-band scattering efficiencies of silicate spheres were similar for grains with radii of 0.2–0.3 μm. Attempts to reconcile the neutral colors of the disk with the 10%–25% polarization of scattered light from the disk have been problematic. Voshchinnikov & Krügel (1999) and Krivova et al. (2000) found that although the polarization alone is best fitted with a grain size distribution with a lower limit of a few microns, the observed neutral colors can only be replicated by adding submicron-sized grains and lowering either the refractive index of the grains or the proportion of the smallest grains. Given the adjustments needed to match the polarization models with the highly uncertain disk colors, a more precise multicolor imaging study of the β Pic disk is warranted.

In this paper we present multiband coronagraphic images of β Pic's circumstellar disk obtained with *HST*'s Advanced Camera for Surveys (ACS; Ford et al. 2003; Gonzaga et al. 2005). These images reveal the disk between 30 and 300 AU from the star with unprecedented spatial resolution, scattered-light suppression, and photometric precision. These qualities permit the measurement of the disk's optical colors with 3–10 times better precision than previously reported from ground-based observations. By deconvolving the instrumental point-spread function (PSF) from each image, we accurately determine the brightnesses, morphologies, and asymmetries of the two disk components associated with the warp in the inner disk. Our fully processed images and results will likely serve as the empirical standards for subsequent scattered-light models of the inner disk until the next generation of space-based coronagraphic imagers is deployed.

2. OBSERVATIONS AND DATA PROCESSING

2.1. *ACS Imaging Strategy and Reduction*

Multiband coronagraphic images of the A5 V star β Pic were recorded on UT 2003 October 1 using the High Resolution Channel (HRC) of ACS (Ford et al. 2003; Gonzaga et al. 2005). The HRC features a 1024×1024 pixel CCD detector whose pixels subtend an area of $0\rlap{.}''028 \times 0\rlap{.}''025$, providing a $\sim29'' \times 26''$ field of view (FOV). Beta Pic was acquired in the standard "peak-up" mode with the coronagraph assembly deployed in the focal plane of the aberrated beam. The star was then positioned behind the small ($0\rlap{.}''9$ radius) occulting spot located approximately at the center of the FOV. *HST* was oriented so that the disk's midplane appeared approximately perpendicular to the $5''$ occulting finger and the large ($1\rlap{.}''5$ radius) occulting spot that also lie in the FOV. Short, medium, and long exposures were recorded through the F435W (*B*), F606W (broad *V*), and F814W (broad *I*) filters over three consecutive *HST* orbits. All images were digitized using the default analog-to-digital conversion of 2 e^- DN^{-1}. This sequence of exposures was promptly repeated after rolling *HST* about the line of sight by $\sim10°$. This offset changed the orientation of the disk in the FOV by $\sim10°$ and facilitated the discrimination of features associated with the disk from those intrinsic to the coronagraphic PSF. Immediately before the exposures of β Pic, coronagraphic images of the A7 IV star

TABLE 1
LOG OF ACS/HRC EXPOSURES

Star	Roll Angle[a] (deg)	Orbit	Filter	Exposures (s)
α Pic	87.2	1	F435W	1×40
		1	F435W	2×100
		1	F435W	2×225
		1	F606W	1×15
		1	F606W	2×50
		1	F606W	2×200
		1	F814W	1×40
		1	F814W	2×100
		1	F814W	2×200
β Pic	110.0	2	F606W	1×10
		2	F606W	2×100
		2	F606W	6×338
		3	F435W	1×10
		3	F435W	2×250
		3	F435W	3×653
		4	F814W	1×10
		4	F814W	2×250
		4	F814W	3×645
β Pic	100.3	5	F606W	1×10
		5	F606W	2×100
		5	F606W	6×338
		6	F435W	1×10
		6	F435W	2×250
		6	F435W	3×653
		7	F814W	1×10
		7	F814W	2×250
		7	F814W	3×645

NOTE.— Recorded over seven consecutive *HST* orbits on UT 2003 October 1.
[a] Defined as the position angle of the *y*-axis of the raw HRC image, measured east of north.

FIG. 1.—$29'' \times 10''$ sections of the F606W (broad *V*) images of β Pic (*top, middle*) and the reference star α Pic (*bottom*) obtained with the ACS/HRC coronagraph. The images are displayed with logarithmic scaling but without correction of geometric distortion. The dust disk around β Pic, which is viewed nearly edge-on, is evident without subtraction of the stellar PSF. The apparent position angles of the disk in the top and middle panels change in accordance with the *HST* roll offset of $9°.7$. The linear feature seen in all three panels is a component of the coronagraphic PSF, whose origin is currently unknown. It is collinear with the HRC's occulting finger, which lies beyond the FOV of each panel.

α Pic were recorded through the same filters to provide reference images of a star having colors similar to those of β Pic but no known circumstellar dust. A log of all HRC exposures is given in Table 1.

The initial stages of image reduction (i.e., subtraction of bias and dark frames and division by a noncoronagraphic flat field) were performed by the ACS image calibration pipeline at the Space Telescope Science Institute (STScI; Pavlovsky et al. 2005). To correct the vignetting caused by the occulting spots, we divided the images by normalized "spot flats" that were appropriately registered to the approximate locations of the migratory occulting spots on the date of our observations (Krist et al. 2004). We then averaged the constituent images of each set of exposures listed in Table 1 after interpolating over static bad pixels and eliminating transient bad pixels with a conventional 3σ rejection algorithm. We then normalized the averaged images to unit exposure time and replaced saturated pixels in the long-exposure images with unsaturated pixels at corresponding locations in the shorter exposure images. Throughout this process, we tracked the uncertainties associated with each image pixel. In this manner we created cosmetically clean, high-contrast images and meaningful error maps for each combination of star, filter, and roll angle. Figure 1 shows $29'' \times 10''$ sections of the reduced F606W images of β Pic and α Pic obtained at each roll angle.

2.2. *Subtraction of the Coronagraphic PSF*

To distinguish the brightness and morphology of the disk from the diffracted and scattered light of β Pic, the occulted star's PSF must be removed from each image. By observing α Pic and β Pic in cons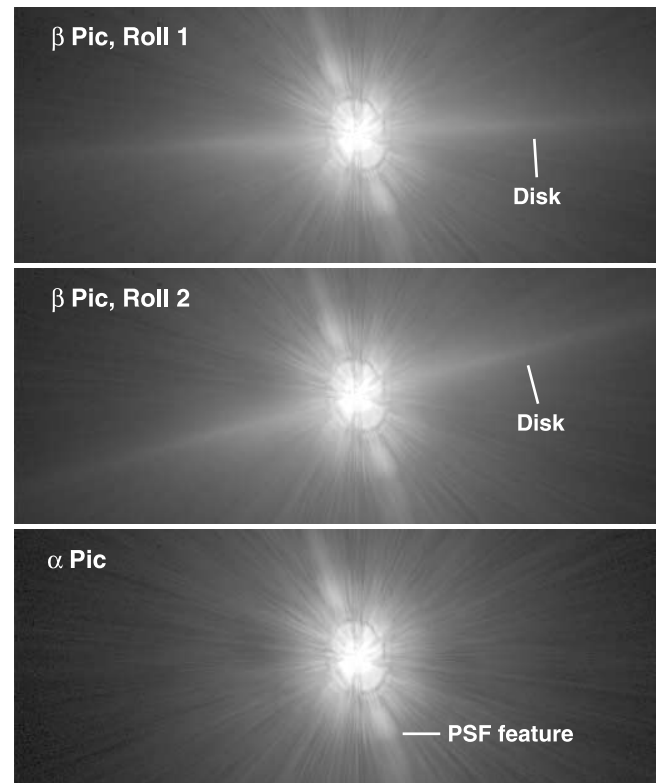ecutive *HST* orbits, we limited the differences between the coronagraphic PSFs of the two stars that would otherwise be caused by inconsistent redeployment of the coronagraph assembly, gradual migration of the occulting spot, or changes in *HST*'s thermally driven focus cycles (Krist 2002). We measured the positions of the stars behind the occulting spot using the central peaks of the reduced coronagraphic PSFs (Fig. 1) that result from the reimaging of incompletely occulted, spherically aberrated starlight by ACS's corrective optics (Krist 2000). The positions of β Pic and α Pic differed by ~ 0.8 pixels ($\sim 0''.02$). This offset causes large differences between the coronagraphic PSFs in the immediate vicinity of the occulting spot, but the residual light at larger field angles ($\gtrsim 5''$ from the star) after PSF subtraction is $\sim 10^{3.5}$ times fainter than the disk's midplane at those field angles (Krist 2000).

Optimal subtraction of the coronagraphic PSF requires accurate normalization and registration of the filter images of the reference star α Pic with the corresponding images of β Pic. Because direct images of the two stars were not obtained, we estimated the brightnesses of each star in each ACS bandpass using the *HST* synthetic photometry package Synphot, which has been developed and distributed by STScI (Bushouse et al. 1998). In doing so we used the optical spectra of the A5 V stars θ^1 Serpentis and Praesepe 154 (Gunn & Stryker 1983) to approximate the spectrum of β Pic. Likewise, we approximated the spectrum of α Pic with that of the A5 IV star HD 165475B. These proxies yielded synthetic Johnson-Cousins photometry that closely matches the Cousins *BVRI* measurements of α Pic and β Pic reported by Bessel (1990). Assuming *V* magnitudes of 3.27 and 3.86 for α Pic and β Pic, respectively, we computed synthetic flux ratios
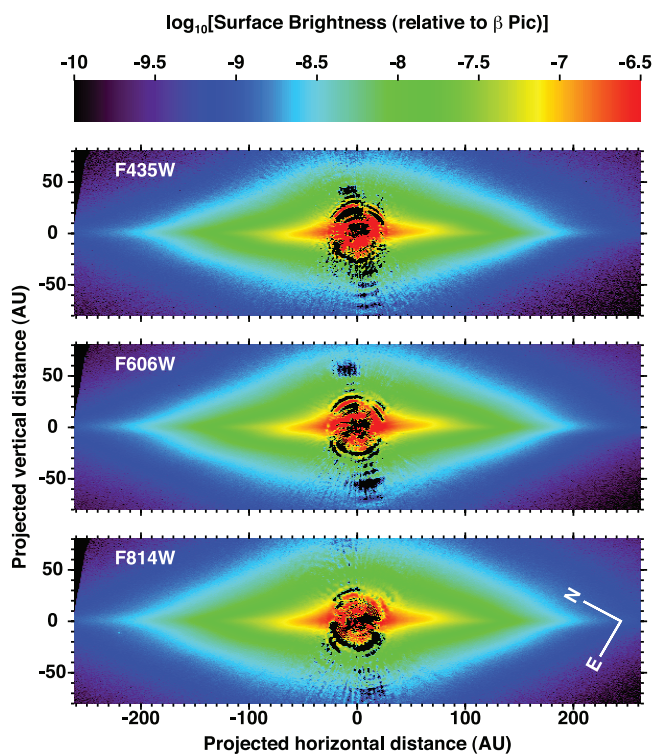
FIG. 2.—Multiband HRC images of the disk around β Pic after subtraction of the stellar PSF but before deconvolution of the off-spot PSF. The panels show $27\rlap{.}''2 \times 8\rlap{.}''3$ sections of the F435W (B), F606W (broad V), and F814W (broad I) images. The image sections have been rotated so that the northeast extension of the disk appears to the left of each panel and the midplane of the outer disk (radius $\gtrsim 100$ AU) is horizontal. Each color-coded panel shows the logarithm of the disk's surface brightness relative to the star's brightness in that bandpass. The irregular, blackened regions near the center of each panel reflect imperfect PSF subtraction around the occulting spot, especially along the direction of the occulting finger, which is beyond the exhibited FOV.

FIG. 3.—Same as Fig. 2, but with the vertical scale expanded by a factor of 4. The color-coded images represent the surface brightnesses of the disk relative to those measured along the spine of the disk. (See § 2.2 for details.) The expanded vertical scale exaggerates the warp in the inner region of the disk first reported by Burrows et al. (1995). The red dot seen to the left of the "NE" label in the bottom panel is a very red background source located $11\rlap{.}''5$ from β Pic at a position angle of $32\rlap{.}°0$.

F_α/F_β of 1.65, 1.75, and 1.90 for F435W, F606W, and F814W, respectively. We then divided the images of α Pic by these ratios to bring the integrated brightnesses of the reference PSFs into conformity with those of β Pic.

We aligned the normalized images of α Pic with the corresponding images of β Pic using an interactive routine that permits orthogonal shifts of an image with subpixel resolution and cubic convolution interpolation. The shift intervals and normalization factors (i.e., F_α/F_β) were progressively refined throughout the iterative process. We assessed the quality of the normalization and registration by visually inspecting the difference image created after each shift or normalization adjustment. Convergence was reached when the subtraction residuals were visibly minimized and refinements of the shift interval or normalization factor had inconsequential effects. Based on these qualitative assessments, we estimate that the uncertainty of the registration along each axis is 0.125 pixels and the uncertainty of F_α/F_β in each bandpass is 2%.

After subtracting the coronagraphic PSFs from each image, we transformed the images to correct the pronounced geometric distortion in the HRC image plane. In doing so we used the coefficients of the biquartic-polynomial distortion map provided by STScI (Meurer et al. 2002) and cubic convolution interpolation to conserve the imaged flux. We then combined the images obtained at each HST roll angle by rotating the images of the second group clockwise by $9\rlap{.}°7$ (Table 1), aligning the respective pairs of images according to the previously measured stellar centroids and averaging the image pairs after rejecting pixels that exceeded
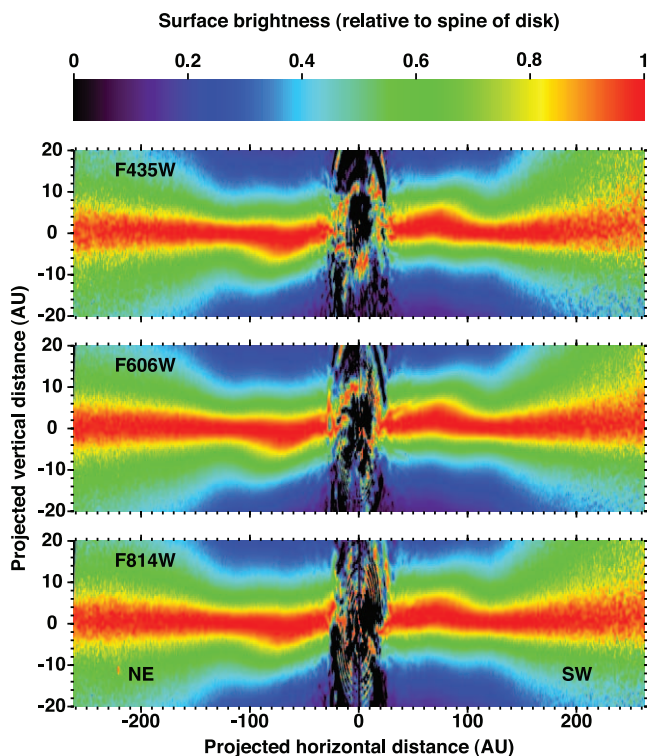
their local 3 σ values. Again, we tracked the uncertainties associated with each stage of image processing to maintain a meaningful map of random pixel errors.

We combined in quadrature the final random-error maps with estimates of the systematic errors caused by uncertainties in the normalization and registration of the reference PSFs. Other systematic errors from cyclic changes of HST's focus and differences between the field positions and broadband colors of α Pic and β Pic are negligible compared with the surface brightness of β Pic's disk over most of the HRC's FOV (Krist 2000). Our systematic-error maps represent the convolved differences between the optimal PSF-subtracted image of β Pic and three nonoptimal ones generated by purposefully misaligning (along each axis) or misscaling the images of α Pic by amounts equal to our estimated uncertainties in PSF registration and F_α/F_β. The total systematic errors are $1-5$ times larger than the random errors within $\sim 3''$ of β Pic, but they diminish to 10%–25% of the random errors beyond $\sim 6''$ of the star. We refer to the combined maps of random and systematic errors as total-error maps.

Figure 2 shows the reduced and PSF-subtracted images of the disk in each ACS bandpass. Each image has been rotated so that the northeast extension of the disk is displayed horizontally to the left of each panel. The images have been divided by the brightness of β Pic in each bandpass derived from Synphot.[23]

---

[23] All calibrated surface brightnesses and colors presented in this paper are based on the following Vega-based apparent magnitudes for β Pic obtained from Synphot: $m_{F435W} = 4.05$, $m_{F606W} = 3.81$, and $m_{F814W} = 3.68$. The systematic zero-point errors are <2% (Sirianni et al. 2005), and the estimated errors from imperfectly matched reference spectra are $\sim 1\%–2\%$.
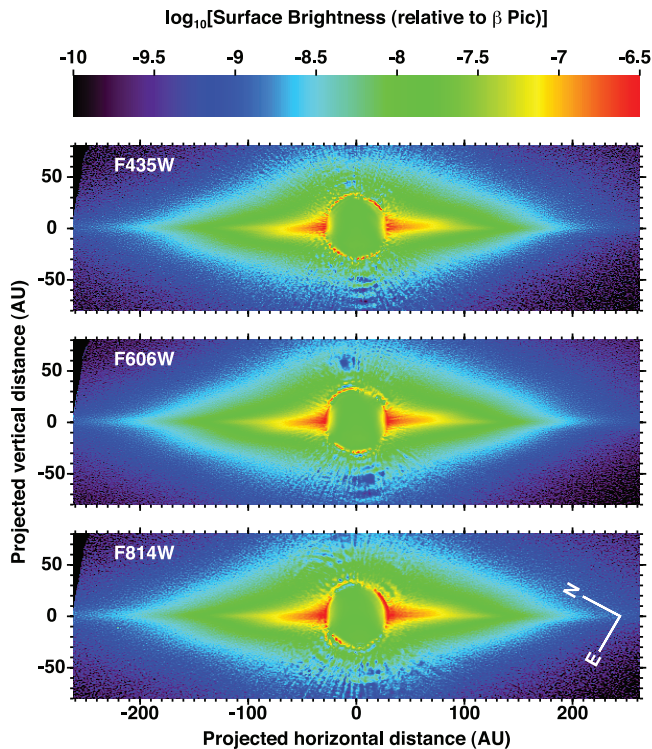
FIG. 4.—Same images as in Fig. 2 after Lucy-Richardson deconvolution of the off-spot PSF. Pixels lying within a radius of 1$\farcs$5 ($\sim$30 AU) of the image center (i.e., the location of the occulted star) have been masked and excluded from the deconvolution. Because the Lucy-Richardson algorithm forces all pixels to have positive values, the deconvolved images exhibit no negative PSF-subtraction residuals and enhanced, correlated noise at faint signal levels. Consequently, photometry of the disk in these regions of the disk is less reliable than in regions having large S/N ratios and small subtraction residuals.
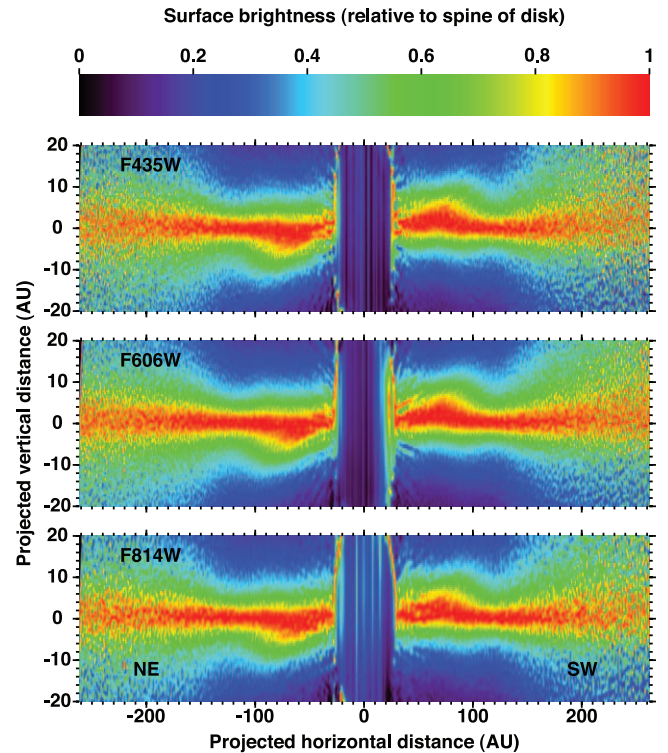
FIG. 5.—Same images as in Fig. 3 after Lucy-Richardson deconvolution of the off-spot PSF. The color-coded isophotes are more similar among these deconvolved filter images than among the convolved images shown in Fig. 3. Side effects of the deconvolution process are described in Fig. 4.

The alternating light and dark bands near the occulting spot reflect imperfect PSF subtraction caused by the slightly mismatched colors and centroids of α Pic and β Pic. The bands perpendicular to the disk have amplitudes that are $\sim$50%–100% of the midplane surface brightnesses at similar distances from β Pic. These residuals preclude accurate photometry of the disk within 1$\farcs$5 ($\sim$30 AU) of the star and anywhere along the direction of the occulting finger. Along the midplane of the disk, the photometric uncertainties due to PSF subtraction are $\sim$5%–10% at a radius of $r = 30$ AU and less than 1% for $r > 60$ AU.

Figure 3 shows alternate views of the disk in which the vertical scale is expanded by a factor of 4 over that presented in Figure 2 and the vertical dimension of the disk's surface brightness is normalized by the brightness measured along the "spine" of the disk. (The spine comprises the vertical locations of the maximum disk brightness measured along the horizontal axis of each image, after smoothing with a 3×3 pixel boxcar.) The expanded vertical scale exaggerates the warp in the inner disk first observed in images taken with HST's Wide Field Planetary Camera 2 (WFPC2) by Burrows et al. (1995). The multiband images shown in Figures 2 and 3 can be directly compared with the unfiltered optical image of the disk obtained with the Space Telescope Imaging Spectrograph (STIS) coronagraph (Grady et al. 2003) and shown in Figure 8 of Heap et al. (2000).

2.3. Deconvolution of the "Off-Spot" PSF

Accurate assessment of the chromatic dependencies of the disk's color and morphology requires the deconvolution of the unoccluted instrumental PSF from each HRC filter image. This deconvolution of the "off-spot" PSF is especially important for the F814W images, because very red photons ($\lambda \gtrsim 0.7\,\mu$m) passing through the HRC's CCD detector are scattered diffusely from the CCD substrate into a large halo that contributes significantly to the wide-angle component of the PSF (Sirianni et al. 2005). Unfortunately, no collection of empirical off-spot reference PSFs exists yet for the HRC coronagraph. Consequently, we can deconvolve the off-spot PSFs only approximately by using synthetic PSFs generated by the Tiny Tim software package distributed by STScI (Krist & Hook 2004). Tiny Tim employs a simplistic model of the red halo that does not consider its known asymmetries (Krist et al. 2005b), but this model is sufficient for assessing the general impact of the red halo on our images of β Pic's disk.

We generated model off-spot PSFs using the optical prescriptions, filter transmission curves, and sample A5 V source spectrum incorporated in Tiny Tim. For simplicity we approximated the weakly field-dependent PSF in each bandpass with single model PSFs characteristic of the center of the FOV. The model PSFs extended to an angular radius of 10$''$. We corrected the geometrically distorted model PSFs in the manner described in § 2.2, and then deconvolved them from the PSF-subtracted images of β Pic obtained at each roll angle. In doing so we applied the Lucy-Richardson deconvolution algorithm (Richardson 1972; Lucy 1974) to each image outside a circular region of radius 1$\farcs$5 centered on the subtracted star. (The amplitudes and spatial frequencies of the PSF-subtraction residuals within this region were too large to yield credible deconvolved data.) The imaged FOV lacked any bright point sources by which we could judge convergence of the deconvolution, so we terminated the computation after 50 iterations. Examination of intermediate stages of the process showed no perceptible change in the deconvolved images after $\sim$45 iterations.

Figures 4 and 5 are the deconvolved counterparts of Figures 2 and 3, respectively. The compensating effect of the deconvolution is especially evident when comparing the morphologies of the disk in Figures 3 and 5. The color-coded isophotes of the disk in each bandpass are much more similar in the deconvolved images than in the convolved images. The amplified, correlated noise in the deconvolved images is characteristic of the Lucy-Richardson algorithm when applied to faint, extended sources. It is a consequence of the algorithm's requirements of a low background signal, nonzero pixel values, and flux conservation on both local and global scales. These requirements also account for the disappearance of the negative PSF-subtraction residuals near the occulting spot. The requirement of local flux conservation ensures reliable photometry in regions where the ratio of signal to noise (S/N) is large and where PSF-subtraction residuals are small, but it makes photometric measurements elsewhere less accurate and their uncertainties nonanalytic.

3. IMAGE ANALYSIS

The processed ACS/HRC images shown in Figures 2 and 3 are the finest multiband, scattered-light images of β Pic's inner disk obtained to date.[24] Earlier ground-based, scattered-light images show the usual effects of coarse spatial resolution and PSF instability caused by variable atmospheric and local conditions (Smith & Terrile 1984; Paresce & Burrows 1987; Golimowski et al. 1993; Lecavelier des Etangs et al. 1993; Kalas & Jewitt 1995; Mouillet et al. 1997a, 1997b). The unpublished $BVRI$ WFPC2 images of the disk described by Burrows et al. (1995) have comparatively low S/N ratios because WFPC2 lacks a coronagraphic mode, and directly imaged starlight scatters irregularly along the surface of its CCD detectors. These conditions forced short exposure times to avoid excessive detector saturation and created irreproducible artifacts in the PSF-subtracted images. Moreover, the construction of a WFPC2 reference PSF from images of β Pic obtained at several roll angles allowed possible contamination of the reference PSF by the innermost region of the disk. The unfiltered STIS images of the disk (Heap et al. 2000) compare favorably with our HRC images, notwithstanding their lack of chromatic information and partial pupil apodization (Grady et al. 2003). Both sets of images show the same region of the disk, although STIS's narrow occulting wedge permitted imaging of the disk's midplane about 0″.4 (8 AU) closer to the star. The HRC's circular occulting spot and Lyot stop exposed the regions around the projected minor axis of the disk that were obscured in the STIS images by diffraction spikes and the shadow of the occulting bar. The HRC images have twice the spatial resolution of the STIS images, and they exhibit better S/N ratios in the regions of the disk between 150 and 250 AU from the star.

3.1. Disk Morphology

Figure 6 shows isophotal maps of our F606W images of the disk before and after deconvolution of the off-spot PSF. These maps are qualitatively similar to those generated from our F435W and F814W images. They confirm the morphology and asymmetries of the disk reported previously by several groups and described in detail by Kalas & Jewitt (1995) and Heap et al. (2000). The brightness asymmetry between the disk's opposing exten-
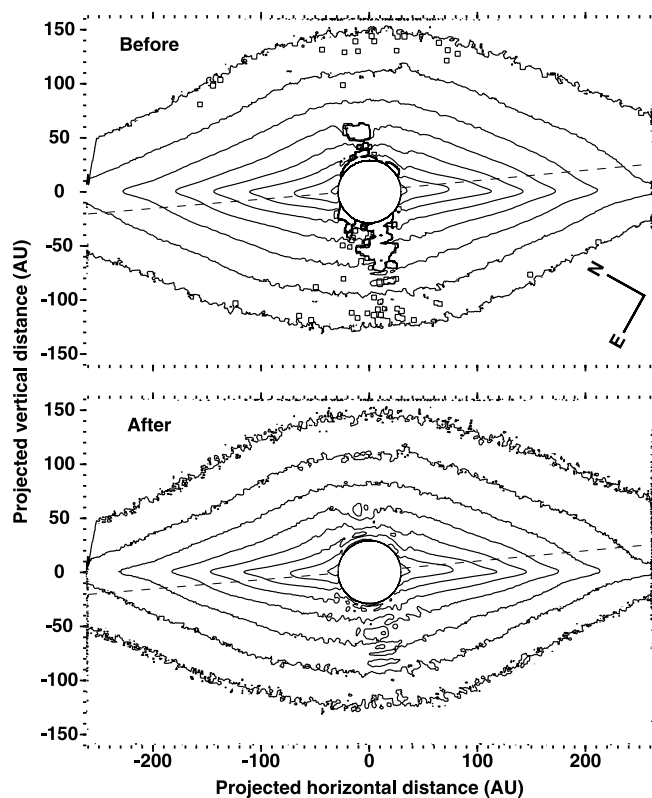
FIG. 6.—Isophotal map of our F606W images of the disk before (*top*) and after PSF deconvolution (*bottom*). The images were smoothed with a 9×9 pixel boxcar. The interval between isophotes is 1 mag arcsec^{-2}; the outermost isophote in each panel marks a surface brightness of 20 mag arcsec^{-2}. A circular mask of radius 1″.5 ($\sim$30 AU) has been imposed on the innermost region of the disk to reduce confusion from PSF-subtraction residuals. Each dashed line represents the least-squares fit to the midplane of the corresponding extension of the inner, secondary disk (see § 3.1.1).

sions is particularly evident along the spine beyond $\sim$100 AU of β Pic. The asymmetric curvature of the isophotes on opposite sides of the spine and the inversion of this asymmetry across the projected minor axis of the disk are also apparent. Kalas & Jewitt (1995) referred to this diametrical antisymmetry as the "butterfly asymmetry."

Our images provide the first credible look at the surface brightness along the disk's projected minor axis. The convex isophotes in this region indicate that the pinched appearances of the disk in the images of Smith & Terrile (1984), Golimowski et al. (1993), Lecavelier des Etangs et al. (1993), Mouillet et al. (1997a, 1997b), and, to a lesser degree, Kalas & Jewitt (1995) are artifacts of oversubtraction of the reference PSF and/or self-subtraction of the disk along its minor axis. Other scattered-light images yielded no information in this region because of obscuration by coronagraphic masks (Paresce & Burrows 1987; Gledhill et al. 1991; Heap et al. 2000). Our images are tinged by residuals from the imperfect subtraction of the linear PSF feature seen in Figure 1, but these residuals do not affect the overall contours of the isophotes. The isophotes are more widely spaced along the northwestern semiminor axis than along the southeastern semiminor axis. Such brightness asymmetry in optically thin disks is often attributed to the enhanced forward-scattering efficiency of the dust, which implies that the side of the disk closer to Earth is inclined slightly northwest from the line of sight to the star. This deduction is consistent with the inclination determined by Kalas & Jewitt (1995) from single-scattering models of the surface brightness along the projected major axis of the disk.
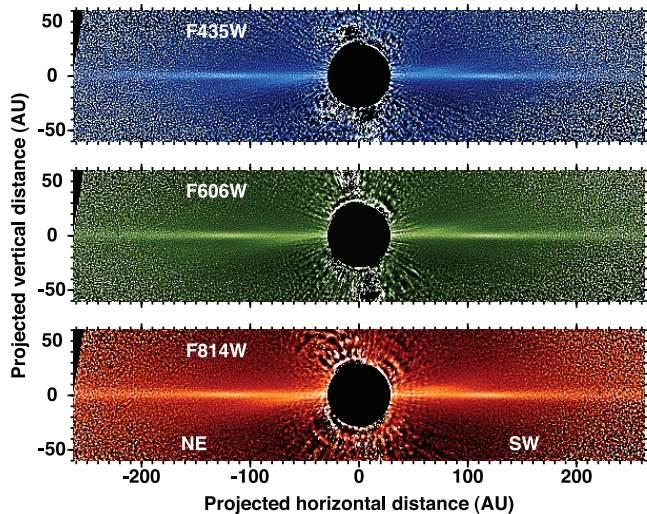
Fig. 7.—Ratios of HRC filter images after and before deconvolution of the off-spot coronagraphic PSF (i.e., images in Fig. 4 divided by the corresponding images in Fig. 2). These images accentuate the sharply peaked midplane of the disk and support the notion that the inner warp is a secondary disk, distinct from the main outer disk and inclined from it by ∼5°. A circular mask of radius 1″5 (∼30 AU) has been imposed on the innermost region of the disk to reduce confusion from PSF-subtraction residuals.

3.1.1. *The Main and Secondary Disks*

Mouillet et al. (1997b) viewed the inner warp as a deformed and thickened region of the disk, perhaps caused and sustained by a planet in an inclined, eccentric orbit within 20 AU of β Pic. Heap et al. (2000) subsequently interpreted the warp as a blend of two separate disk components, the lesser of which is inclined from the main component by 4°6. The latter interpretation is supported by Figure 7, which shows the ratios of our HRC images after and before deconvolution of the off-spot PSF. The division of the PSF-deconvolved filter images (Fig. 4) by their corresponding convolved images (Fig. 2) accentuates the small or narrow features in the disk that are most affected by blurring from the instrumental PSF. Thus, the sharply peaked midplane of the outer disk appears prominently in Figure 7. The midplane of the inner warp is not as well defined as that of the outer disk, but the apparent separation of the midplanes beyond ∼80 AU from the star indicates that the warp is a distinct secondary disk inclined from, and perhaps originating within, the main disk.

Mimicking Heap et al. (2000) we determined the contributions of the main and secondary disks to the composite vertical scattered-light profile (i.e., the scattered-light distribution perpendicular to the midplane of the disk) by fitting two similar, vertically symmetric profiles to the composite profile as a function of distance from the star. In doing so we assigned a shape to the individual profiles by qualitatively assessing various analytic functions at a few locations along the disk in our PSF-deconvolved images. We found that a "hybrid-Lorentzian" function—two Lorentzians of different widths whose top and bottom parts, respectively, are smoothly joined at an arbitrary distance from their common centers—satisfactorily matched each individual profile. (We ascribe no physical significance to this hybrid-Lorentzian function, nor do we claim that it uniquely or optimally characterizes each profile.) We used a nonlinear least-squares fitting algorithm based on the Levenberg-Marquardt technique (Press et al. 1992) to determine the positions, amplitudes, widths, and top-to-bottom transition zones of the main and secondary hybrid-Lorentzian profiles at distances of 30–250 AU from β Pic. The resulting fits of the composite vertical profiles were best in the
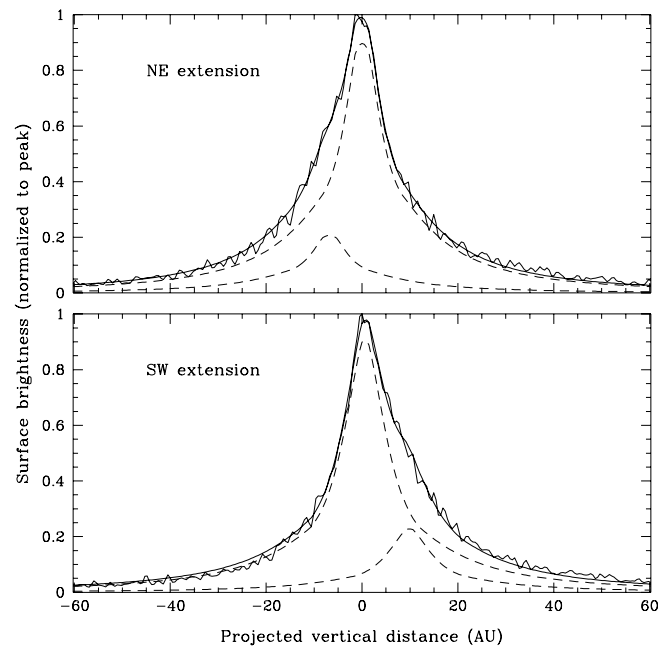

Fig. 8.—Vertical scattered-light profiles (i.e., the scattered-light distributions perpendicular to the midplane) of each extension of the disk at a projected horizontal distance of 100 AU from β Pic. The jagged solid curves are the observed profiles extracted from our F606W images after PSF-deconvolution. Each smooth solid curve is the sum of two hybrid-Lorentzian functions (*dashed curves*; see § 3.1.1) that best fits the respective observed profile. The dashed curves represent the contributions of the main and secondary disks to the composite vertical profile. The asymmetry of each composite profile and the reversal of this asymmetry in opposing extensions of the disk reflect the butterfly asymmetry characterized by Kalas & Jewitt (1995).

regions 80–130 AU from the star, where the two disk components are sufficiently bright and separated to allow unambiguous discrimination of both components. Figure 8 shows the best fits to the composite vertical profiles of both extensions of the disk observed in our F606W image at distances of 100 AU from the star.

Figure 9 shows the relative positions of the fitted components of the composite vertical profile as a function of distance from β Pic. For each filter image and disk extension, we performed linear least-squares fits to the traces of the main and secondary disks within the regions where they are accurately identified (80–250 AU for the main disk and approximately 80–130 AU for the secondary disk). These fits are overplotted in Figure 9. The relative position angles of the main disk's northeast and southwest extensions (measured counterclockwise from the horizontal axis) are about −0°4 and 0°5, respectively. The difference between these position angles is similar to the "wing-tilt asymmetry" noted by Kalas & Jewitt (1995) at distances of 100–450 AU from β Pic. However, our fitted lines appear to intersect at a point almost coincident with the star, rather than at a point in the southwest extension, as reported by Kalas & Jewitt. Expanding the vertical scale of our traces of the main disk in the F606W image (Fig. 10) shows that the spine of the northeast extension conforms to the linear fit down to ∼80 AU, at which point the main and secondary disks can no longer be credibly distinguished. However, the spine of the southwest extension exhibits more curved than linear behavior over the range of the fit. This bow in the southwest extension appears in our F435W and F814W images with equal clarity and therefore does not appear to be an artifact of our decomposition of the vertical scattered-light profile.

Table 2 lists the position angles of the linear fits along each extension of the secondary disk relative to the corresponding fits along the main disk. The average tilt of the secondary disk's
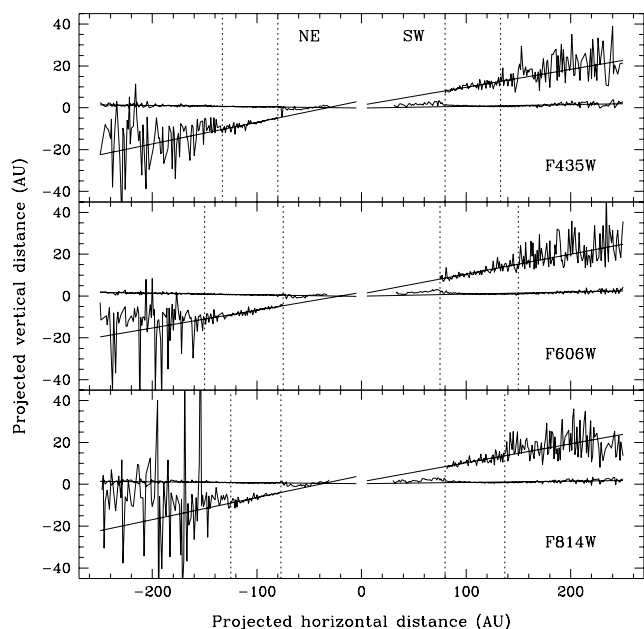
FIG. 9.—Traces of the two hybrid-Lorentzian components of the composite vertical profiles (e.g., Fig. 8) at horizontal distances of 30–250 AU from β Pic. The vertical dotted lines bound the regions where the composite profiles can be accurately decomposed into two profiles associated with the main (horizontal) and secondary (tilted) disks. The solid lines are least-squares fits to the traces along each disk extension in the regions between 80 and 250 AU for the main disk and between the vertical dotted lines for the secondary disk. Profile decomposition breaks down within ~80 AU of the star, as evidenced by the large deviations of the main disk components from their respective linear fits. The noisy traces of the secondary disk within ~80 AU have been omitted for clarity's sake.

southwest extension matches the 4°.6 derived by Heap et al. (2000) for both extensions. However, we find that the average tilt of the northeast extension is ~25% larger than the values obtained by Heap et al. (2000) and by us for the southwest extension. Extrapolating the linear fits to the secondary disk outward (Fig. 6) shows that the convex inflections of the butterfly asymmetry are aligned with the secondary disk, which supports the notion that the asymmetry is caused by radiatively expelled dust
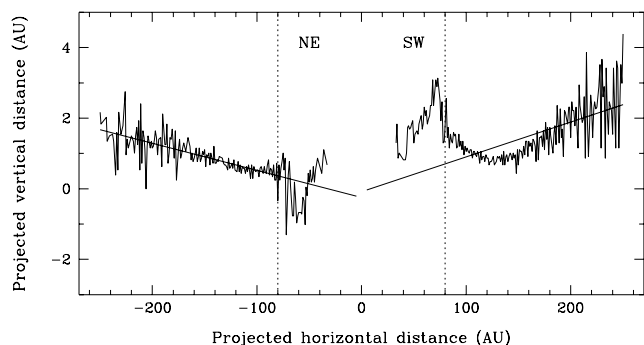

FIG. 10.—Magnified traces of the main disk component observed in our F606W image after PSF deconvolution. The vertical dotted lines mark the 80 AU boundary within which the composite vertical scattered-light profile cannot be credibly decomposed into its main and secondary disk components. The solid lines are the least-squares fits to the traces along each extension of the main disk at distances of 80–250 AU from β Pic. The opposite slopes of the linear fits reflect a persistent but diminished "wing-tilt asymmetry," first noted by Kalas & Jewitt (1995) at large distances from the star. The general conformity of the northeast extension to the linear fit is not observed in the southwest extension. The opposing traces obtained from the F435W and F814W images show similar asymmetry; their average vertical positions deviate from the F606W traces by <0.5 AU (i.e., less than 1 HRC pixel) beyond 80 AU from the star.

TABLE 2
RELATIVE POSITION ANGLES OF THE SECONDARY DISK

Extension	F435W (deg)	F606W (deg)	F814W (deg)	Average (deg)
Northeast	6.3	5.3	6.3	5.9 ± 0.6
Southwest	−4.4	−4.9	−4.8	−4.7 ± 0.3

NOTE.— The position angles pertain to regions of the secondary disk between the vertical dotted lines in Fig. 9 and are measured relative to the corresponding extensions of the main disk.

from the secondary disk (Augereau et al. 2001). On the other hand, extending the linear fits to the secondary disk toward β Pic (Fig. 9) shows that its nonparallel extensions would not converge near the star if they extended sufficiently inward. Instead, the northeast extension would intersect the northeast extension of the main disk at a distance of ~30 AU from β Pic. Coronagraphic images with a smaller occulting spot and higher pixel resolution are needed to determine whether this intersection actually occurs.

Although our analysis of the two-component structure of the disk qualitatively supports that of Heap et al. (2000), our results reveal some errors in the presentation and interpretation of their results. These errors stem from the incorrect portrayal of the secondary disk's tilt relative to the northeast and southwest extensions of the main disk in Figures 11–13 of Heap et al. (2000). In these figures the plotted data, and consequently the relative slope of the secondary disk, are inverted about the midplane of the main disk. The orientations of the main and secondary disks should appear as they do in Figures 7–9 of this paper and in Figures 8 and 10 of Heap et al. (2000). Because of this inversion, Heap et al. concluded that the disk's southeast side was brighter than its northwest side and, consequently, that the southeast side was inclined toward the line of sight. These conclusions are not supported by our isophotal map of the disk (Fig. 6) or by the single-scattering models of Kalas & Jewitt (1995).

3.1.2. Thickness of the Main Disk

Previous scattered-light studies indicated that the composite disk is uniformly thick within 7″ (135 AU) of β Pic and flared beyond that region (Smith & Terrile 1984; Paresce & Burrows 1987; Artymowicz et al. 1990; Golimowski et al. 1993; Kalas & Jewitt 1995; Mouillet et al. 1997a; Heap et al. 2000). These characteristics are evident in Figures 3 and 5. Previous measurements of the disk's full width at half its midplane (FWHM) brightness vary significantly, however, which suggests that the disk's intrinsic projected width is less than or comparable to the resolution of the images from which the measurements were made. Our deconvolution of the off-spot PSF from the HRC images—the first such effort exhibited for scattered-light images of β Pic's disk—permits us to assess this resolution dependency and to measure more accurately the intrinsic width of the disk as a function of distance from β Pic.

Figure 11 shows the full widths of each extension of the composite disk at half and one-tenth of the maximum brightness of the midplane at distances 20–250 AU from the star. These widths are shown in the panels labeled "FWHM" and "FW0.1M," respectively. The associated pairs of thin solid and dashed curves show the widths of the northeast and southwest extensions obtained from the F606W image before and after PSF deconvolution. The short, thick curves show the measured widths of the hybrid-Lorentzian curves that best fit the main component of the composite disk in the region 80–150 AU from β Pic (§ 3.1.1).
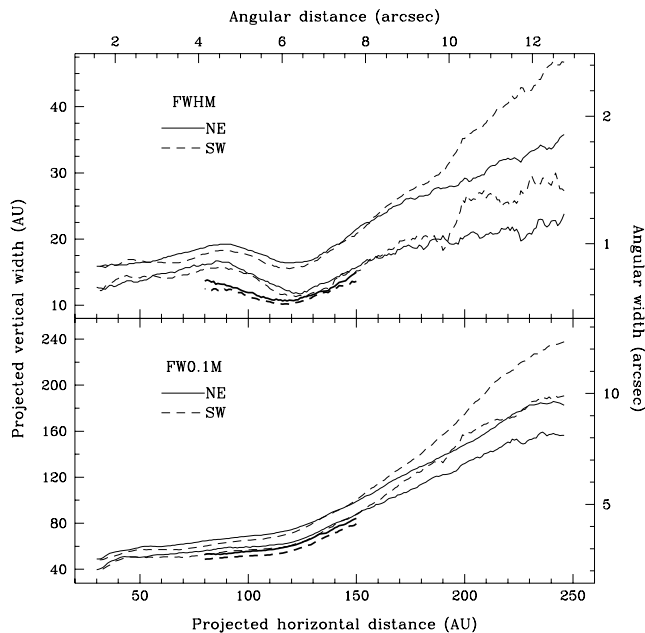
Fig. 11.—Projected vertical width of the composite disk as a function of horizontal distance from β Pic. The curves trace the full widths of each extension of the disk at half (*top*) and one-tenth (*bottom*) of the maximum (midplane) brightness. The upper pair of thin solid and dashed curves in each panel shows the widths of the northeast and southwest extensions, respectively, measured from the F606W image before deconvolution of the off-spot PSF. The lower pair of thin curves shows the reduced widths after PSF deconvolution. The short, thick pair of curves in each panel shows the widths of the main component of the disk between 80 and 150 AU after decomposition and extraction of the tilted secondary disk. All curves have been smoothed with a 9 pixel boxcar.

The FWHM and FW0.1M plots show progressive reductions in the measured width of the main disk after PSF deconvolution and decomposition of the main and secondary disks. The up to 30% reduction in the FWHM after deconvolution of the narrow off-spot PSF (FWHM $\approx 0\rlap{.}''05$) shows that previously reported measurements, particularly those obtained from the ground, reflect more the angular resolution of the observations than the intrinsic thickness of the disk.

The deconvolved and decomposed curves show that the FWHM and FW0.1M of both disk extensions are nearly constant (~11–13 and ~50–60 AU, respectively) within ~120 AU of β Pic, and they increase approximately linearly with distance beyond ~120 AU. This behavior is consistently seen in the F435W, F606W, and F814W images. The southwest extension appears to thicken more rapidly than the northeast extension beyond ~160 AU, as noted by Kalas & Jewitt (1995), but the correlated noise injected into the deconvolved images by the Lucy-Richardson algorithm (Fig. 5) precludes accurate quantification of the FWHMs from those images. Reverting to the PSF-convolved images, we find that the FWHM and FW0.1M of the southwest extension are ~10 and ~60 AU larger, respectively, than the corresponding values of the northwest extension 250 AU from the star. Our finding is consistent with the FWHM measurements of Kalas & Jewitt (1995) when the different angular resolutions of the two sets of observations are considered. Heap et al. (2000) reported no such thickness asymmetry from their STIS images. Their measurements of the FWHM at discrete locations 50–200 AU from β Pic are consistent with our PSF-convolved measurements of the narrower northeast extension. However, their FW0.1M measurements at these locations are 20%–60% smaller than our PSF-convolved measurements at the same locations in each extension. These discrepancies may reflect differences between the S/N

ratios of the HRC and STIS images at scattered-light levels below $\sim10^{-9}$ of the stellar flux.

3.1.3. *Planetesimal Belts or Rings*

Reexamining earlier WFPC2 and ground-based coronagraphic images of β Pic, Kalas et al. (2000) noted several localized density enhancements along the midplane of the disk's northeast extension at distances of 500–800 AU from the star. They did not see this structure in the southwest extension, so they interpreted the clumps as a system of eccentric, nested rings formed in the aftermath of a close encounter between the disk and a passing star. Wahhaj et al. (2003) and Weinberger et al. (2003) later reported mid-infrared images of the disk that show a distinct warp within 20 AU of the star that is oppositely tilted from the secondary disk seen in Figure 7. Wahhaj et al. (2003) also noted clumps of emission in both disk extensions within 100 AU of β Pic that are arranged in diametrically opposite pairs centered on the star. They interpreted these clumps as a series of noncoplanar rings caused by gravitational interactions of the disk with a planetary system. Telesco et al. (2005) did not observe the innermost warp in their mid-infrared images of the disk, but they attributed a bright clump of 12–18 μm emission at 52 AU in the southwest extension to a concentration of 0.1–0.2 μm silicate and organic refractory grains heated to ~190 K. High-spatial-resolution, mid-infrared spectra of the disk recorded at 3 AU intervals along the inner 30 AU of each extension also show concentrated regions of emission from 0.1–2 μm silicate grains (Okamoto et al. 2004). The presence of such concentrations of small grains in the face of expulsive stellar-radiation pressure suggests that the grains are continuously created by collisions of planetesimals confined to rings or belts within the otherwise depleted inner region of the dust disk.

The bright clumps detected by Kalas et al. (2000) in the northeast extension of the disk lie outside the FOV of our HRC images, and the innermost warp reported by Wahhaj et al. (2003) and Weinberger et al. (2003) is obscured by the HRC's occulting spot. However, the clumps of mid-infrared emission located 30–100 AU from the star (Wahhaj et al. 2003; Telesco et al. 2005) are potentially observable in our HRC images. Figure 12 is an isophotal map of the inner region of the disk obtained from our PSF-deconvolved F606W image after smoothing with a 3×3 pixel boxcar. The isophotal interval is 0.2 mag arcsec^{-2}, which is similar to the interval between isophotes of 18 μm emission from the same region of the disk presented by Wahhaj et al. (2003) and Telesco et al. (2005). The locations of the clumps of 18 μm emission are marked with the letters assigned to them by Wahhaj et al. Our F606W isophotes show no evidence of such clumping in scattered optical light. Adjusting the isophotal interval and the smoothing factor does not alter this conclusion. Our images do not refute the existence of the clumps, however, because the scattered optical light and mid-infrared emission may emanate from different regions of the disk (Pantin et al. 1997).

3.2. *Surface Brightness and Asymmetry*

Because β Pic's disk is viewed nearly edge-on, its surface brightness has traditionally been parameterized with one or more power laws fitted along the midplanes (or spines) of its opposing extensions (Smith & Terrile 1984; Artymowicz et al. 1989, 1990; Gledhill et al. 1991; Golimowski et al. 1993; Lecavelier des Etangs et al. 1993 ; Kalas & Jewitt 1995; Mouillet et al. 1997a; Heap et al. 2000). The number of fitted power laws and their indices have varied considerably, mostly because such fits are sensitive to errors in the stellar PSF subtraction. The innate stability of *HST*'s instrumental PSFs reduces these errors substantially,
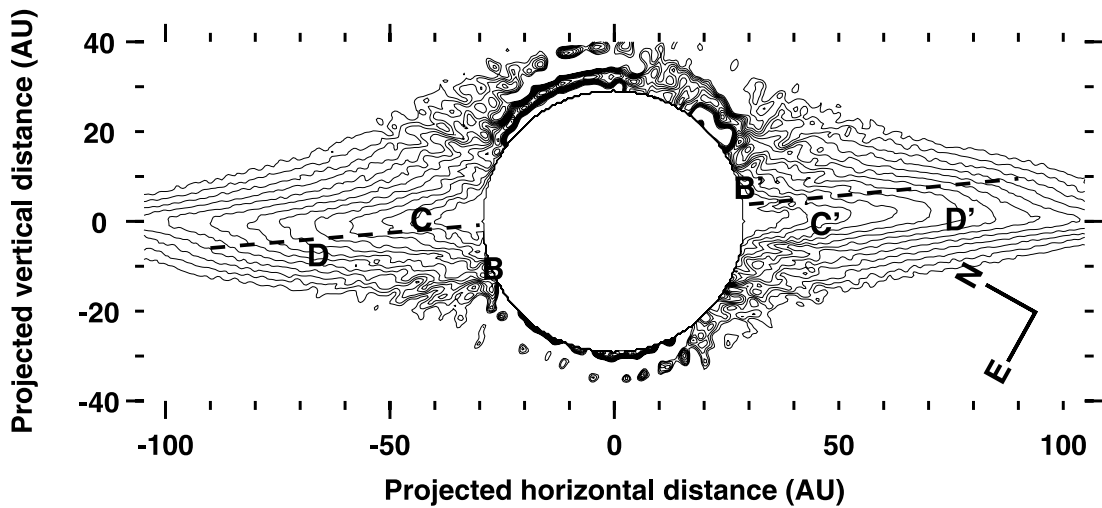
Fig. 12.—Isophotal map of the inner region of the disk obtained from our PSF-deconvolved F606W image. The data have been smoothed with a 3 × 3 pixel boxcar. The isophotes represent surface brightnesses of 10–15.4 mag arcsec^{-2} at intervals of 0.2 mag arcsec^{-2}. The dashed lines are the best linear fits to the spine of the secondary disk. The locations of the diametrically opposed clumps of 18 μm emission are marked with the letters assigned to them by Wahhaj et al. (2003). The bright clump of emission reported by Telesco et al. (2005) is nearly coincident with clump C′. No such clumping is evident in scattered optical light.

Fig. 13.—Multiband surface brightness profiles measured along the spine of each disk extension before PSF deconvolution. The dotted curves are ±1 σ error profiles derived from the total-error maps of the images (§ 2.2) and ~3% uncertainty in the photometric calibration. The dashed lines are least-squares fits to the logarithmic data at angular distances of 2″–3″.5, 3″.7–5″.6, 6″.6–10″, and 10″–13″.4 from β Pic. The slopes of these lines (i.e., the indices of the equivalent power-law fits) are given in Table 3. The vertical lines at ~1″.5 mark the inner limit of credible photometry.

so we compare our quantitative measurements of the disk's spine (as defined in § 2.2) with those obtained from the STIS images of Heap et al. (2000). To do so, we assess the surface brightnesses of the spines of both extensions from our ACS images both before and after PSF deconvolution. We initially ignore the two-component structure of the disk described in § 3.1.1, because the two components cannot be distinguished by our profile-fitting algorithm within 80 AU of the star (§ 3.1.1) and because the main disk dominates the surface brightness beyond 80 AU. We then compare our results for the composite disk with those obtained for its main and secondary components over the region in which they are credibly resolved.

3.2.1. *Horizontal Profiles of the Composite Disk*

Figure 13 shows the logarithmic surface brightness profiles measured along the spines of each extension of the composite disk before PSF deconvolution. The accompanying $\pm 1\ \sigma$ error profiles, which are derived from the total-error maps of the images (§ 2.2) and include $\sim$3% uncertainty in the photometric calibration, show that these profiles are very accurate beyond $\sim$1″5 ($\sim$30 AU) from the star. The profiles clearly do not indicate a single power-law dependence of surface brightness with distance, as was determined in some of the earliest ground-based imaging studies of the disk (Smith & Terrile 1984; Artymowicz et al. 1989; Gledhill et al. 1991; Lecavelier des Etangs et al. 1993). Instead, the logarithmic profiles exhibit distinctly different linear behavior at angular distances of 2″–3″5, 3″7–5″6, 6″6–10″, and 10″–13″4, with smooth transitions in slope between these regions. Table 3 lists the slopes of the linear least-squares fits to the logarithmic data (i.e., the indices of the radial power laws, $r^{-\alpha}$, that best fit the surface brightness profiles) within these four regions. The prominent changes in α at $\sim$6″ ($\sim$115 AU) from the star are well documented (Artymowicz et al. 1990; Golimowski et al. 1993; Kalas & Jewitt 1995; Heap et al. 2000), but the more subtle changes at $\sim$3″6 ($\sim$70 AU) and $\sim$10″ ($\sim$195 AU) are noted here for the first time. Conversely, the pronounced decrease in the disk's B-band surface brightness within 7″3 ($\lesssim$140 AU) reported by Lecavelier des Etangs et al. (1993) is not observed in our F435W image.

The prominent inflections in the profiles at $\sim$115 AU are possible evidence for the sublimation of water ice from composite grains at dust temperatures greater than 100–150 K (Nakano 1988; Artymowicz et al. 1990; Golimowski et al. 1993; Pantin et al. 1997; Li & Greenberg 1998). Applying their cometary dust model to β Pic's disk, Li & Greenberg (1998) noted that the relative compositions of the grains should vary across several regions of the disk, as the inner and outer mantles of various ices and organic refractory material successively evaporate from, or condense on, their silicate cores in accordance with the local dust temperature and stellar-radiation pressure. The more subtle changes in α at $\sim$70 and $\sim$195 AU may therefore mark the boundaries over which such changes in composition (and consequently albedo) occur. On the other hand, the decrease in α within $\sim$70 AU may indicate a decrease in the number density of the grains caused by an interior planetary system (Lagage & Pantin 1994; Roques et al. 1994; Lazzaro et al. 1994) or, as we discuss in § 3.2.2, the unresolved superposition of the main and secondary disks.

The changes in α at angular distances of $\sim$3″6, 6″, and 10″ from β Pic are also apparent in the midplane surface brightness profiles extracted from the STIS images of the disk (Heap et al. 2000). To facilitate comparison with previous studies, Heap et al. fitted power-law functions to three regions of each extension. Two of these regions coincide approximately with our regions 1 and 3 defined in Table 3; the third region bridges our regions 1 and 2.

TABLE 3
POWER-LAW FITS TO SURFACE BRIGHTNESS PROFILES OF THE COMPOSITE DISK

PSF DECON?	REGION[a]	POWER-LAW INDEX (α)[b]		
		F435W	F606W	F814W
Northeast Extension				
No	1	1.34 ± 0.02	1.34 ± 0.02	1.30 ± 0.02
	2	1.91 ± 0.02	1.91 ± 0.02	1.90 ± 0.02
	3	4.28 ± 0.02	4.19 ± 0.02	4.04 ± 0.02
	4	3.51 ± 0.07	3.63 ± 0.04	3.49 ± 0.06
Yes	1	1.45 ± 0.04	1.43 ± 0.03	1.38 ± 0.03
	2	1.84 ± 0.04	1.83 ± 0.03	1.80 ± 0.03
	3	4.20 ± 0.05	4.19 ± 0.04	4.12 ± 0.04
	4[c]	2.80 ± 0.15	3.34 ± 0.11	3.34 ± 0.12
Southwest Extension				
No	1	1.02 ± 0.02	1.06 ± 0.02	1.15 ± 0.02
	2	2.03 ± 0.02	2.03 ± 0.02	2.05 ± 0.02
	3	4.89 ± 0.03	4.76 ± 0.02	4.56 ± 0.02
	4	3.99 ± 0.09	4.00 ± 0.05	3.84 ± 0.07
Yes	1	1.08 ± 0.04	1.10 ± 0.03	1.21 ± 0.04
	2	1.93 ± 0.04	1.94 ± 0.03	1.97 ± 0.03
	3	4.82 ± 0.06	4.75 ± 0.05	4.60 ± 0.05
	4[c]	3.11 ± 0.18	3.53 ± 0.12	3.26 ± 0.14

[a] Angular and projected distances of regions from β Pic: (1) 2″0–3″5 (39–67 AU); (2) 3″7–5″6 (71–108 AU); (3) 6″6–10″0 (127–193 AU); (4) 10″0–13″4 (193–258 AU).
[b] Index of the radial power law, $r^{-\alpha}$, that best fits the surface brightness of the spine within a given region of each disk extension. Equivalently, $-\alpha$ is the slope of the linear least-squares fit to the given region of the logarithm of the profile, as shown in Fig. 13.
[c] Indices in region 4 of the PSF-deconvolved images are suspect because the efficacy of the Lucy-Richardson algorithm is diminished in regions of low S/N ratio.

Our values of α in region 1 (2″–3″5 or 39–67 AU from β Pic) of both extensions differ by $\lesssim$5% from those computed by Heap et al. (2000) for the positions of maximum flux along each extension. However, our values of α in region 3 (6″6–10″ or 127–193 AU from β Pic) are $\sim$10%–15% smaller than those of Heap et al. for both extensions; i.e., our power-law fits in this region are significantly less steep than those determined from the STIS images. This discrepancy is puzzling, especially as this outer region of the disk is relatively insensitive to moderate errors in the PSF subtraction.

To investigate the possible effect of the convolved instrumental PSF on our power-law fits, we repeated this analysis on our PSF-deconvolved images in each bandpass. The surface brightness profiles along the spines of each deconvolved disk extension are shown in Figure 14. The corresponding values of α for each region of the deconvolved images are listed in Table 3. These values are significantly different from their PSF-convolved counterparts only in region 4, where the S/N ratios are low and, consequently, the efficacy of the Lucy-Richardson algorithm is suspect. In region 3 the average difference between the associated convolved and deconvolved indices is $\sim$1%, so it is unlikely that differences between the HRC and STIS coronagraphic PSFs cause the $\sim$10%–15% discrepancies in the values of α reported by Heap et al. (2000) and us for this region.

Figure 15 displays the PSF-deconvolved profiles in a manner that facilitates comparison of the two disk extensions in the F435W, F606W, and F814W images. The plots show the effects of the asymmetric values of α on the relative brightnesses of the two extensions at equal distances from β Pic. The southwest
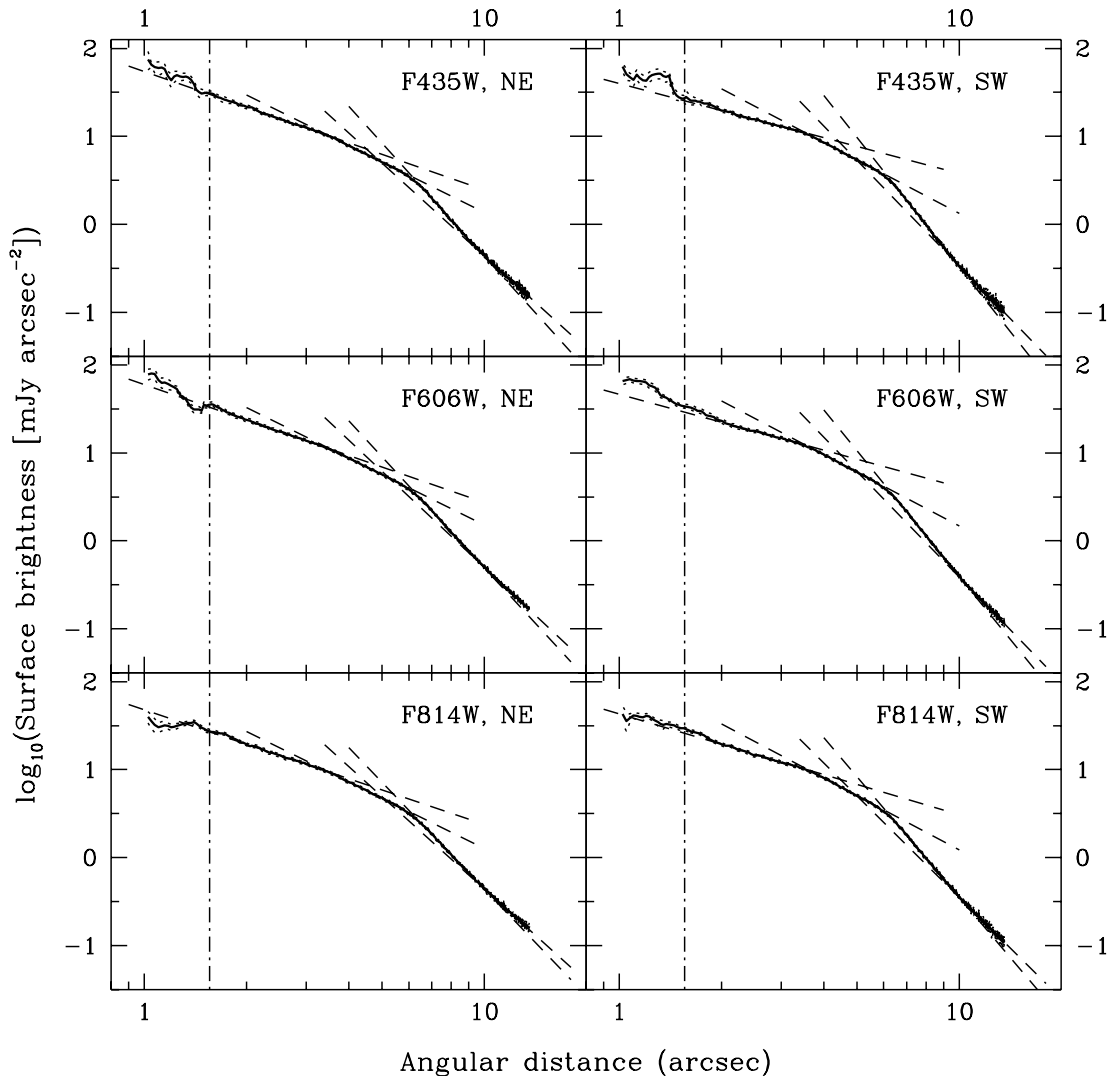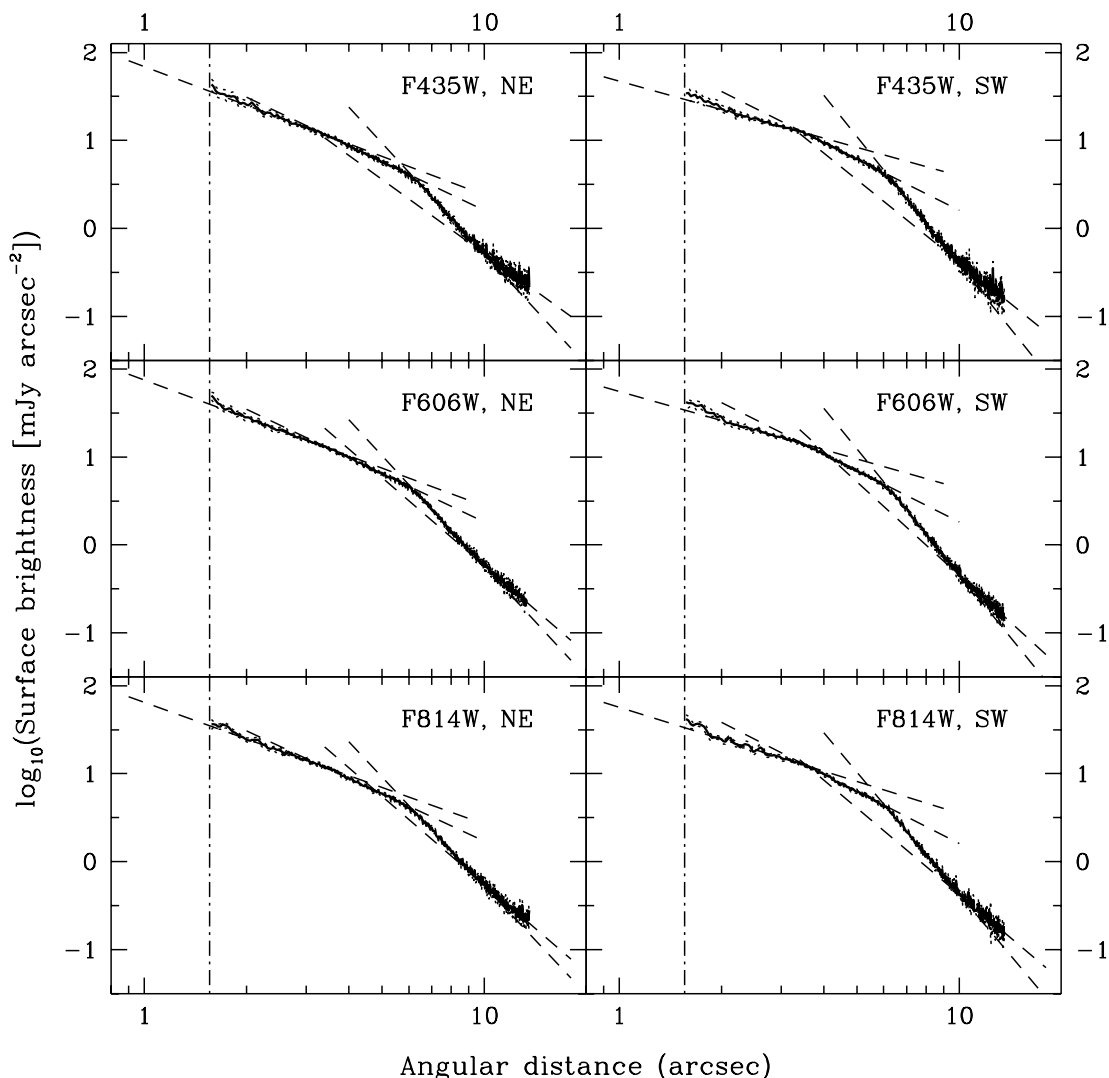
Fig. 14.—Multiband surface brightness profiles measured along the spine of each disk extension after PSF deconvolution. The dotted curves are ±1 σ error profiles obtained by combining in quadrature the ±1 σ errors of the PSF-convolved images (Fig. 13) and local estimates of the correlated noise imparted by the Lucy-Richardson algorithm. The dashed lines are least-squares fits to the logarithmic data for the regions described in Fig. 13; their slopes are given in Table 3. The vertical lines at ∼1″.5 mark the boundary of the circular pixel mask used during PSF deconvolution.

extension is brighter than the northwest extension in the region ∼50–100 AU from the star, whereas the opposite condition exists for $r \gtrsim 150$ AU. At $r = 6''$ (∼115 AU), the surface brightness of each extension is 14.9, 14.6, and 14.4 mag arcsec^{-2} in F435W, F606W, and F814W, respectively. These values are 0.2–0.3 mag arcsec^{-2} brighter than the corresponding brightnesses measured from the PSF-convolved images. The latter measurements compare favorably with the ground-based, R-band measurements of Golimowski et al. (1993) and Kalas & Jewitt (1995) at $r = 6''$ but are ∼1.5 mag arcsec^{-2} brighter than the R- and I-band measurements reported by Paresce & Burrows (1987) and Smith & Terrile (1984), respectively, for this fiducial distance. The outer distance limits of our photometric measurements (260 and 300 AU for the northeast and southwest extensions, respectively) are set by the HRC's FOV; they do not reflect an intrinsic asymmetry in the physical sizes of the extensions.

Although the values of α within ∼110 AU of β Pic (regions 1 and 2) are nearly constant across F435W, F606W, and F814W, those between 125 and 200 AU (region 3) decrease nonuniformly with increasing wavelength. These trends indicate that the optical colors of the disk are constant within ∼110 AU of the star, but they redden considerably between 125 and 200 AU. The

color gradient appears to flatten again from ∼200 to 250 AU (region 4), but the relatively large uncertainties attached to α in this region preclude a definitive assessment. We confirm these trends in our subsequent analysis of the disk's color (§ 3.3).

3.2.2. Horizontal Profiles of the Component Disks

The resolution of the inner disk into two components prompts an assessment of the contributions of each component to the horizontal surface brightness profiles of the composite disk. Figure 16 shows the multiband, logarithmic profiles of the main and secondary disks, extracted from the PSF-deconvolved images. The curves trace the maxima of the hybrid-Lorentzian profiles that best fit the vertical surface brightness profiles of the two disks at 80–150 AU from β Pic (§ 3.1.1). The secondary disk is ∼1.5 mag arcsec^{-2} fainter than the main disk at 100 AU, as indicated in Figure 8. The profiles of the main disk show the same inflections at ∼6″ (∼115 AU) exhibited by the composite disk, but the secondary disk's profiles appear linear throughout this region. Whereas the relative brightnesses of the main disk's extensions invert at ∼115 AU (as noted in § 3.2.1 for the composite disk), the southwest extension of the secondary disk is consistently brighter than its northeast extension from 80 to 150 AU.
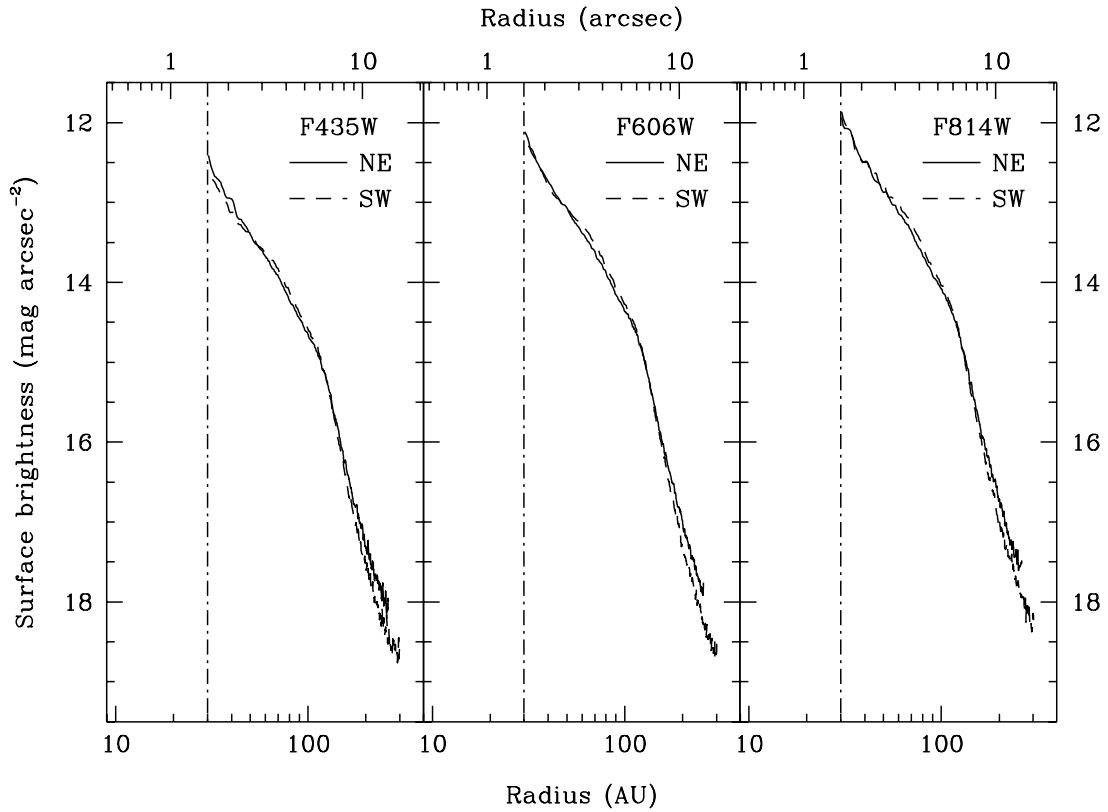
FIG. 15.—Multiband surface brightness profiles measured along the spine of each disk extension after PSF deconvolution. The data have been smoothed with a 5 pixel boxcar to improve clarity. The dashed lines at 30 AU mark the boundary of the circular pixel mask used during PSF deconvolution. The uncertainty in the photometric calibration of each bandpass is ~0.03 mag.

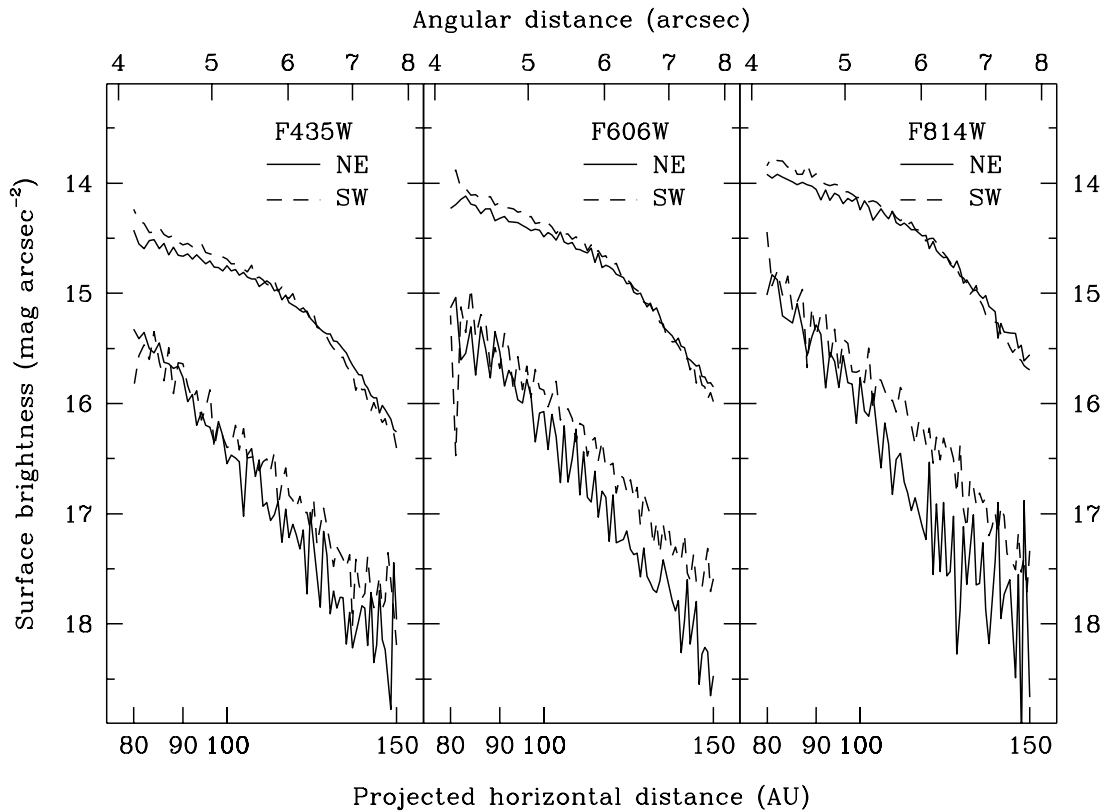FIG. 16.—Multiband surface brightness profiles of the main (*top*) and secondary (*bottom*) disk components, obtained from the PSF-deconvolved images. The unsmoothed curves trace the maxima of the hybrid-Lorentzian profiles that best fit the vertical profiles of the two components between 80 and 150 AU from β Pic (see § 3.1.1). The uncertainty in the photometric calibration of each bandpass is ~0.03 mag.

TABLE 4
POWER-LAW FITS TO SURFACE BRIGHTNESS PROFILES OF THE COMPONENT DISKS

| | | REGION | REGION | POWER-LAW INDEX (α) | | |
EXTENSION	COMPONENT	(arcsec)	(AU)	F435W	F606W	F814W
Northeast	Main	4.1–5.6	80–108	1.23 ± 0.06	1.42 ± 0.07	1.19 ± 0.08
	Main	6.6–7.8	127–150	5.09 ± 0.12	4.52 ± 0.11	4.38 ± 0.25
	Secondary	4.1–7.8	80–150	4.46 ± 0.14	4.63 ± 0.14	4.97 ± 0.24
Southwest	Main	4.1–5.6	80–108	1.50 ± 0.05	1.64 ± 0.06	1.58 ± 0.06
	Main	6.6–7.8	127–150	5.23 ± 0.16	5.18 ± 0.14	4.96 ± 0.12
	Secondary	4.1–7.8	80–150	3.80 ± 0.10	3.72 ± 0.13	3.93 ± 0.10

NOTE.—Profiles are extracted from the PSF-deconvolved images and shown in Fig. 16.

We fitted power laws to the profiles of both extensions of the main and secondary disks over the regions displayed in Figure 16, taking care to avoid the inflection of the main disk at ~115 AU. Table 4 lists the indices, α, of these power laws. The main disk's indices at 80–108 AU are 15%–35% smaller than those of the composite disk in the mostly overlapping region 2 (defined in Table 3), whereas its indices at 127–150 AU are 5%–20% larger than those of the composite disk in region 3. These indices are nearly constant across F435W, F606W, and F814W at 80–108 AU, but they progressively decrease with increasing wavelength at 127–150 AU. This behavior mimics that of the composite disk in regions 2 and 3 (§ 3.2.1), which indicates that the main disk's colors progressively redden beyond the inflection at ~115 AU. Conversely, the secondary disk's indices progressively increase with increasing wavelength within the entire 80–150 AU region of the northeast extension, but they are effectively constant in the southwest extension. The former trend suggests that the colors in the northeast extension become bluer with increasing distance from β Pic. Altogether, these characteristics indicate that the grain populations and/or distributions in the main and secondary disks differ significantly at common projected distances from the star. Moreover, if unresolved, the secondary disk can significantly affect models that use the scattered-light profiles to constrain the spatial distribution and composition of dust in the main disk.

3.3. Optical Colors of the Disk

Previous multiband-imaging studies of β Pic's disk showed that the optical colors of the star and disk are indistinguishable within the studies' estimated photometric errors (Paresce & Burrows 1987; Lecavelier des Etangs et al. 1993). These errors ranged from 20% to 30%, so actual color differences of a few tenths of a magnitude would not have been deemed credible. The greater photometric precision of our ACS study enables a correspondingly more precise assessment of the disk's optical colors and scattering properties. We first examine the ACS colors of the composite disk to enable a comparison with the earlier ground-based studies. We then examine the colors of the main and secondary components derived from our decomposition of the disk's vertical scattered-light profile (§ 3.1.1).

3.3.1. Two-Band Flux Ratios of the Composite Disk

Figure 17 shows the F606W/F435W and F814W/F435W flux ratios of the disk obtained from the PSF-deconvolved images shown in Figure 4. Because the images in Figure 4 are separately normalized by the stellar flux in each bandpass, the images in Figure 17 represent the flux ratios of the disk relative to those of the star. Consequently, regions of the disk having a flux ratio of 1.0 exhibit the same $m_{F435W} - m_{F606W}$ and $m_{F435W} - m_{F814W}$

colors (hereafter denoted F435W − F606W and F435W− F814W) as β Pic itself. Although the flux ratios along the projected minor axis of the disk are obscured by the residual artifacts of the PSF subtraction, those along the projected major axis are clear and uncorrupted. The images show that the flux ratios are asymmetric about both projected axes, with the largest ratios appearing in the north-northeast quadrant of the disk. Within ~150 AU of the star, the F606W/F435W and F814W/F435W ratios on the southeast side of the disk are ~1.0–1.1 times those of the star, while the ratios on the northwest side are ~1.2–1.4 times those of the star. The uncertainties of these ratios range from ~5%–10% along the spine to ~25% at projected vertical distances of ±50 AU from the spine. Beyond ~150 AU from the star, the color asymmetry between the two sides diminishes substantially, but the uncertainties away from the spine are comparatively large (~25%–75%).

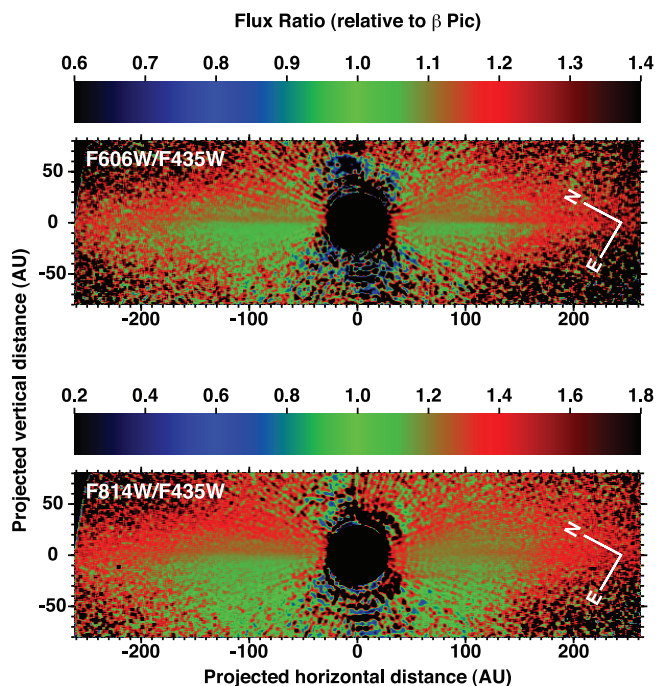Figures 6 and 17 show that the northwest side of the disk within ~150 AU of β Pic is both brighter and redder than its

FIG. 17.—F606W/F435W and F814W/F435W ratio images of the composite disk after PSF deconvolution. The images have been smoothed with a 7×7 pixel boxcar. The flux ratios are measured relative to those of the star in the respective bandpasses. Within 150 AU of the star, the uncertainties in the flux ratios range from ~5% to 10% along the spine of the disk to ~25% at projected distances of ±50 AU from the spine. The F814W/F606W image is not shown but is qualitatively similar to the F606W/F435W and F814W/F435W images.

southeast counterpart. If the brightness asymmetry indicates that the side of the disk nearer to Earth is tipped northwesterly (§ 3.1), then the color asymmetry within ∼150 AU indicates that the ensemble of dust grains in that region becomes increasingly forward-scattering with increasing wavelength. This behavior is inconsistent with the expected scattering properties of both compact and porous interstellar grains (Draine & Lee 1984; Wolff et al. 1998; Voshchinnikov et al. 2005), so its cause is not evident.

The vertical asymmetry of the composite disk's colors is strikingly well aligned with the spine of the disk, which appears prominently in both panels of Figure 17. As the S/N ratios of our flux measurements are largest along the spine, we hereafter restrict our analysis of the disk's colors to that region in order to assess their dependence on the horizontal projected distance from the star. Focusing on the spine also allows us to assess the impact of PSF convolution on the colors measured along this narrow feature of the composite disk.

3.3.2. Colors along the Spine of the Composite Disk

Figure 18 shows the F435W − F606W and F435W − F814W colors of the composite disk relative to those of β Pic, before and after deconvolution of the off-spot PSF. We measured the colors along the spines of each disk extension after smoothing the F606W/F435W and F814W/F435W ratio images with a 7 × 7 pixel boxcar. Although the PSF-convolved colors are less accurate than their deconvolved counterparts, their uncertainties are more suitably compared with those from previous studies in which PSF deconvolution was not performed. The average uncertainties of both colors before PSF deconvolution are ∼3% at 40–150 AU and ∼8% at 150–250 AU, i.e., 3–10 times better than those obtained in previous studies (Paresce & Burrows 1987; Lecavelier des Etangs et al. 1993). PSF deconvolution increases the differences between the F435W − F606W and F435W − F814W colors of the disk and star by ∼0.03 and ∼0.1 mag, respectively, at the cost of increased uncertainty. The relatively large increase in Δ(F435W − F814W) is due to the correction of blurring from both the instrumental PSF and the HRC's red-halo anomaly (§ 2.3). The general similarity of the respective solid and dashed curves in Figure 18 shows that the color variations as a function of distance from β Pic are not significantly affected by PSF deconvolution. This condition is consistent with the practically invariant power-law indices that parameterize the midplane surface brightness profiles in regions 1–3 of the composite disk before and after PSF deconvolution (Table 3).

The PSF-deconvolved curves in Figure 18 show that the F435W − F606W and F435W − F814W colors of the disk are ∼0.1 and ∼0.2 mag redder, respectively, than those of β Pic at distances of ∼40–120 AU from the star. These color excesses are nearly constant within this region and have average uncertainties of ∼8%. The F435W − F606W and F435W − F814W excesses respectively increase to ∼0.2 and ∼0.35 mag at 250 AU in the northeast extension and to ∼0.25 and ∼0.4 mag at 250 AU in the southwest extension. The average uncertainties of both excesses beyond 150 AU from the star are ∼23%, i.e., ∼0.05–0.09 mag at 250 AU. The constancy of F435W − F606W and F435W − F814W within ∼120 AU is consistent with the chromatically invariant power-law indices associated with regions 1 and 2 of the composite disk (Table 3). Likewise, the steadily reddening colors from ∼120 to 250 AU are consistent with the inverse proportionality of α and the wavelength in region 3 of the disk.

Our results contradict the long-standing notion that β Pic's disk scatters visible light neutrally and uniformly. Its red opti-
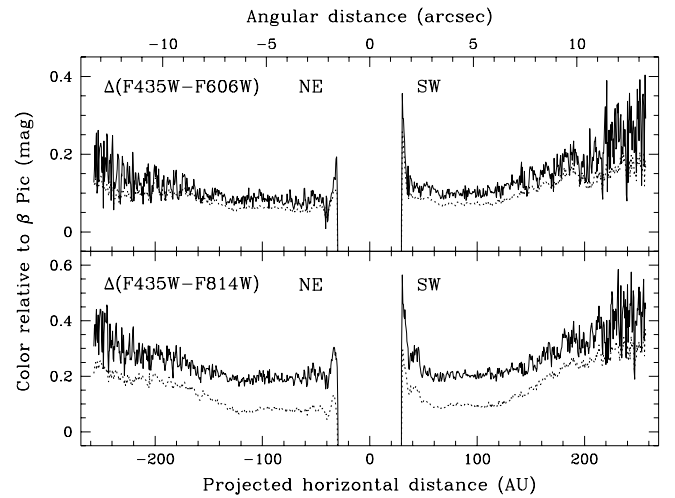

Fig. 18.—F435W − F606W and F435W − F814W colors of the composite disk relative to those of β Pic, obtained before (*dotted curves*) and after (*solid curves*) PSF deconvolution. The disk's colors were measured along the spines of each extension. The ratios of the filter images were smoothed with a 7 × 7 pixel boxcar for improved clarity. The uncertainties of both colors before PSF deconvolution are ∼3% at 40–150 AU and ∼8% at 150–250 AU, whereas those after PSF deconvolution are ∼8% at 40–150 AU and ∼23% at 150–250 AU.

cal colors (relative to the star) are generally consistent with the colors of the disks surrounding the B9 Ve star HD 141569A (Clampin et al. 2003) and the G2 V star HD 107146 (Ardila et al. 2004, 2005), although those disks do not exhibit spatial color gradients such as those seen in β Pic's disk beyond ∼120 AU. The relatively red colors of β Pic's disk contrast markedly with the relatively blue colors of the edge-on disk surrounding AU Microscopii (Krist et al. 2005a), an M dwarf in a comoving group of stars that includes β Pic (Barrado y Navascués et al. 1999; Zuckerman et al. 2001). In § 4.2.6 we speculate that the disparate colors of the disks surrounding β Pic and AU Mic may be caused by small differences between the minimum sizes of dust grains in the two disks.

3.3.3. Colors along the Spines of the Component Disks

Figure 19 shows the F435W − F606W and F435W − F814W colors of each extension of the main and secondary disks in the region 80–150 AU from β Pic. The colors are derived from the maxima of the hybrid-Lorentzian profiles that best fitted these components of the vertical scattered light profiles of the composite disk (§ 3.1.1). Because the colors depend on the robustness of our fitting algorithm at each position along the spine of the composite disk, their uncertainties cannot be analytically determined. We estimate these uncertainties from the rms deviations computed for each disk extension. For the main disk, $\sigma_{(F435W-F606W)} \approx \sigma_{(F435W-F814W)} \approx 0.02$ over both extensions. For the secondary disk, $\sigma_{(F435W-F606W)} \approx 0.1$ over both extensions, and $\sigma_{(F435W-F814W)} \approx 0.1$ and 0.2 over the southwest and northeast extensions, respectively.

The colors of the main disk conform to those of the composite disk between 80 and 150 AU, as expected from its nearly fivefold superiority in brightness over the secondary disk. The colors of the secondary disk's southwest extension also match those of the main disk, but its northeast extension appears bluer than the main disk by ∼0.1–0.2 mag in F435W − F606W and ∼0.1–0.4 mag in F435W − F814W. Moreover, the F435W − F814W color of this extension apparently becomes bluer with increasing distance from the star, as previously suggested by its steepening midplane surface brightness gradient (§ 3.2.2 and Table 4). However, the
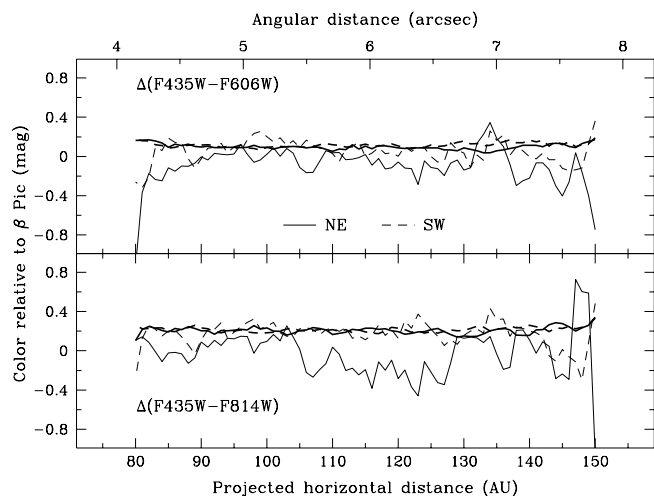
Fig. 19.—F435W − F606W and F435W − F814W colors of the northeast (*solid curves*) and southwest (*dashed curves*) extensions of the main (*thick curves*) and secondary (*thin curves*) disks, relative to the colors of β Pic. The colors are determined from the PSF-deconvolved images using the maxima of the hybrid-Lorentzian profiles fitted to the main and secondary disks 80–150 AU from the star (§ 3.1.1). The data have been smoothed with a 3 pixel boxcar for clarity. The rms deviations of the colors in the main and secondary disks are 0.02 and 0.1–0.2 mag, respectively.

relatively large uncertainties in this region of the disk preclude a definitive assessment of the colors and trends of the secondary disk. Within our estimated errors, the colors of the secondary disk are also consistent with being neutral and constant between 80 and 150 AU.

4. DISCUSSION

4.1. *Impact of PSF Deconvolution on Observations and Models*

Our analysis demonstrates that PSF deconvolution is an important step toward accurately characterizing thin debris disks viewed edge-on or, more generally, less inclined disks having narrow or compact structural elements. It is especially important for multiband imaging studies designed to map the chromatic dependencies of a disk's morphology and surface brightness. For example, PSF deconvolution dispels the illusion that β Pic's disk thickens with increasing wavelength (Figs. 3 and 5) by restoring the displaced red flux to its original location along the disk's spine. This restoration of the true surface brightness distribution contributes largely to our observation that the main disk component is significantly redder than previously determined from ground-based measurements (Paresce & Burrows 1987; Lecavelier des Etangs et al. 1993). It also provides refined empirical constraints for past and future dynamical models that alternatively view the inner warp as a uniform, propagating deformation of a single disk or as two distinctly separate, inclined disks (Mouillet et al. 1997b; Augereau et al. 2001).

The improved measurements of the disk's morphology and surface brightness obtained from our PSF-deconvolved images provide a basis for improved scattered-light models of β Pic's disk. However, deriving the spatial distribution and scattering properties of dust in an edge-on disk is complicated by the integrated effects of variations in both characteristics along the line of sight. This complication is compounded by the many asymmetries between the opposing extensions of β Pic's disk and by the existence of an inclined secondary disk. Consequently, three-dimensional scattering models based on axisymmetric dust distributions, such as those previously developed for the disks around β Pic (Artymowicz et al. 1989; Kalas & Jewitt 1995) and AU Mic (Krist et al. 2005a), have limited utility in the face of the morphological and photometric complexity of β Pic's disk revealed by our HRC images.

Multicomponent, nonaxisymmetric models are clearly needed to reproduce the complicated scattered-light distribution associated with β Pic's disk. Development of such models is beyond the scope of this paper, but we identify several issues raised by our observations that should be addressed by future modeling efforts:

1. The horizontal surface brightness profiles of the main disk within ∼150 AU are sensitive to contamination by flux from the secondary disk. Models of the dust distribution within either disk should be based on deconvolved and deblended components of scattered light from both disks.

2. The spines of the opposing extensions of the secondary disk are not collinear. While the misaligned spines of the main disk (the "wing-tilt asymmetry"; Kalas & Jewitt 1995) are attributed to forward scattering from a slightly inclined disk, those of the secondary disk are not as easily explained. The possible optical and/or dynamical causes of this phenomenon need to be explored.

3. The clumpiness noted in mid-infrared images of the disk is not observed in optical scattered light, even though the grains believed responsible for the clumps of mid-infrared emission (Okamoto et al. 2004; Telesco et al. 2005) have sizes commensurate with efficient scattering of optical light. This apparent incompatibility may indicate that the scattered light and thermal emission come from different regions along the line of sight (Pantin et al. 1997). If so, these disparate observations may constrain the mean scattering properties of the grains.

4. The optical colors of the composite disk are asymmetric about both projected axes of the disk. The generally redder and brighter appearance of the northwest half of the disk is inconsistent with the expectation that the dust grains scatter red light more isotropically than blue light. This peculiar behavior may place interesting constraints on the sizes and compositions of the grains throughout the disk.

5. The prominent changes in the horizontal surface brightness profiles and color gradients at ∼115 AU from β Pic suggest that these phenomena may have a common cause. The expected sublimation of water ice from micron-sized grains lying within ∼100 AU of the star (Pantin et al. 1997; Li & Greenberg 1998) is one possible cause, but color variations caused by changes in the grain size distribution must also be investigated.

Although we defer these issues to future theoretical investigations, we partly address the last issue here via a one-dimensional analysis of the colors observed along the spines of the component disks.

4.2. *Colors and Properties of the Dust*

Li & Greenberg (1998) successfully modeled the disk's continuum emission from near-infrared to millimeter wavelengths and its 10 μm silicate emission feature by assuming that the dust is continually replenished by comets orbiting near or falling onto β Pic. In this scenario the cometary dust grains are highly porous aggregates of primitive interstellar dust whose composition, molecular structure, and size and spatial distributions are altered by the stellar radiation environments into which they are sputtered and transported. Li & Greenberg (1998) did not apply this dust model to the disk's appearance in scattered light because the

scattering properties of highly porous grains with appropriate compositions had not been fully determined. Subsequent modeling of these properties (Wolff et al. 1998; Voshchinnikov et al. 2005) now enables us to examine the porous grain model from the perspective of the disk's optical colors.

We begin by deriving a parameter that, in the absence of a detailed three-dimensional model of the disk, links the optical properties of a variety of grains with the colors observed along the spine of the disk. We apply this parameter first to the colors of the composite disk (Fig. 18), as these colors are largely attributable to the main disk and their uncertainties are well established. Afterward, we examine the less certain colors measured for the secondary disk (Fig. 19).

4.2.1. Effective Scattering Efficiency of Midplane Grains

The intensity of singly scattered light measured along the midplane of an optically thin, edge-on disk is

$$I(\epsilon) = \int n(r)\sigma_{\mathrm{sca}}\Phi(\theta)F_0\left(\frac{r}{r_0}\right)^{-2} dx, \tag{1}$$

where ϵ is the angular distance from the star, $n(r)$ is the number density of grains at a distance r from the star, σ_{sca} is the scattering cross section of grains of a given size and composition, $\Phi(\theta)$ is the phase function of the scattering angle θ, F_0 is the stellar flux at an arbitrary radius r_0, and x traverses the disk along the line of sight. The complicated and asymmetric surface brightness profiles of β Pic's disk suggest that $n(r)$ cannot be expressed as a single analytic function throughout the disk. However, constraining $n(r)$ within each region of each disk extension requires a complex modeling effort that is beyond the scope of this paper.

For a less rigorous analysis of the disk's colors, we approximate the surface brightness and number density profiles along the midplanes of both extensions with single radial power laws having fixed indices $-\alpha$ and $-\nu$, respectively. Because the outer radius of the disk is $\gtrsim 1800$ AU (Larwood & Kalas 2001), our lines of sight mostly traverse regions of the disk that lie well beyond the projected distances at which we see prominent inflections in the surface brightness profiles. The effective index α should therefore be biased toward the indices observed in the outer regions of the disk, i.e., $\alpha \approx 4$ (Smith & Terrile 1984; Kalas & Jewitt 1995). Nakano (1990) determined that $\nu = \alpha - 1$ if the observed scattered light originates mostly from dust lying along parts of the lines of sight near β Pic. This condition is valid unless the dust grains are strongly forward-scattering. Some models indicate that the scattered light is dominated by such grains (Pantin et al. 1997), but the relationships between the sizes, compositions, and optical properties of the grains remain uncertain. Assuming for simplicity that the disk comprises grains that are at most moderately forward-scattering, we obtain

$$n(r) = n_0\left(\frac{r}{r_0}\right)^{-3}. \tag{2}$$

Adopting the disk geometry portrayed in Figure 1 of Buitrago & Mediavilla (1986), we rewrite equation (1) as

$$I(\epsilon) = \frac{F_0 n_0 r_0^5}{R^4 \sin^4\epsilon}\int_{\theta_0}^{\pi-\theta_0}\sigma_{\mathrm{sca}}\Phi(\theta)\sin^3\theta\, d\theta, \tag{3}$$

where R is the distance to β Pic and θ_0 is the scattering angle at the outer edge of the disk. The radius of the disk greatly exceeds the FOV of our images, so $\theta_0 \approx 0$. The integral is then solely dependent on the scattering properties of the grains, so we define the grains' effective scattering efficiency as

$$Q_{\mathrm{eff}} = \int_0^\pi Q_{\mathrm{sca}}\Phi(\theta)\sin^3\theta\, d\theta, \tag{4}$$

where $Q_{\mathrm{sca}} = \sigma_{\mathrm{sca}}/\pi a^2$ and a is the grain size (radius). We use a common scattering phase function for small grains,

$$\Phi(\theta) = \frac{1-g^2}{4\pi(1+g^2-2g\cos\theta)^{3/2}}, \tag{5}$$

where g is the scattering asymmetry parameter defined by

$$g = \langle\cos\theta\rangle = \int_{4\pi}\Phi(\theta)\cos\theta\, d\Omega \tag{6}$$

and $d\Omega$ is the unit solid angle (Henyey & Greenstein 1941). Values of $g = -1, 0$, and 1 correspond respectively to backward, isotropic, and forward scattering.

Substituting equation (5) into equation (4) and evaluating the integral, we obtain

$$Q_{\mathrm{eff}} = \frac{Q_{\mathrm{sca}}}{3\pi}\left(1-g^2\right). \tag{7}$$

This result indicates that our view of the edge-on disk is produced by mostly isotropic scatterers, which conforms to our initial assumption that the grains in the disk are not strongly forward-scattering. Its analytic form is a fortunate consequence of our choice of $\nu = 3$, but the bias against forward-scattering grains is maintained for any choice of $\nu > 1$. Both Q_{sca} and g are functions of the dimensionless parameter $x = 2\pi a/\lambda$, where λ is the wavelength of the scattered light. The mean Q_{eff} for grains of size a, weighted by the stellar flux in a given bandpass, is

$$\langle Q_{\mathrm{eff}}\rangle = \frac{\int Q_{\mathrm{eff}}F_\lambda T_\lambda\, d\lambda}{\int F_\lambda T_\lambda\, d\lambda}, \tag{8}$$

where F_λ is the flux spectrum of β Pic and T_λ is the filter transmission profile. We now compare $\langle Q_{\mathrm{eff}}\rangle$ for grains of various compositions and porosities in the ACS B, broad V, and broad I bands.

4.2.2. Dust Grains within the Ice Sublimation Zone

Figure 20 shows $\langle Q_{\mathrm{eff}}\rangle$ as a function of a for the F435W, F606W, and F814W filters and five combinations of porosity and composition. None of these combinations includes icy mantles, so they are applicable only to the region of the disk within the ice sublimation limit ($\lesssim 100$ AU for micron-sized grains; Pantin et al. 1997; Li & Greenberg 1998). Figures 20a and 20b depict $\langle Q_{\mathrm{eff}}\rangle$ for compact (0% porosity) grains composed, respectively, of pure astronomical silicate ("astrosil") and equal parts astrosil and amorphous carbon (graphite). The curves are derived from tabulated values of Q_{sca} and g for each composition based on the work of Draine & Lee (1984).[25] Figures 20c and 20e show $\langle Q_{\mathrm{eff}}\rangle$ for 33% and 90% porous grains with equal amounts of astrosil

---

[25] As of this writing, tabulated values of Q_{sca} and g for compact grains of astrosil and graphite are available on the World Wide Web at http://www.astro .princeton.edu/~draine/dust/dust.diel.html.
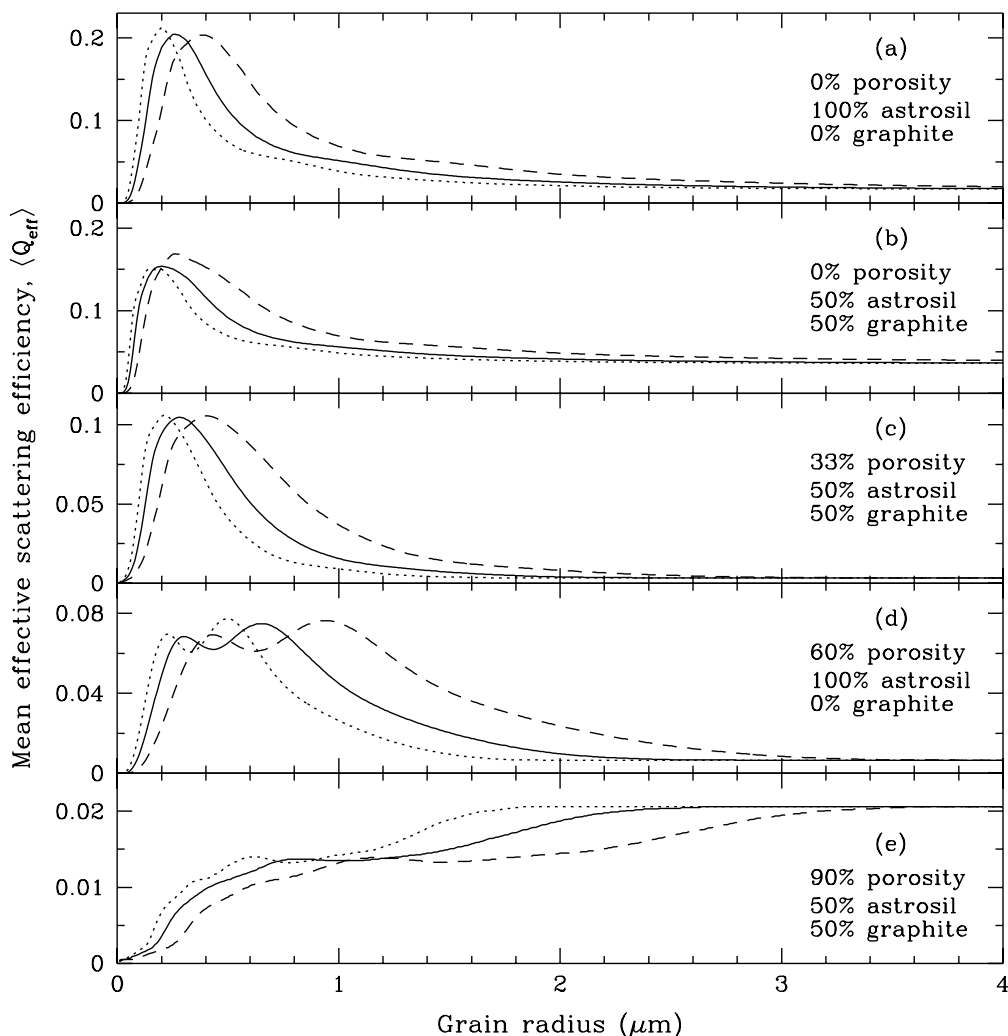
Fig. 20.— $\langle Q_{eff} \rangle$ vs. grain radius for F435W (*dotted curves*), F606W (*solid curves*), and F814W (*dashed curves*) and five combinations of porosity and composition. (*a*) Compact grains of pure astrosil (Draine & Lee 1984). (*b*) Compact grains with equal amounts of astrosil and graphite (Draine & Lee 1984). (*c*) 33% porous grains with equal numbers of astrosil and graphite inclusions (Voshchinnikov et al. 2005). (*d*) 60% porous grains of pure astrosil (Wolff et al. 1998). (*e*) 90% porous grains with equal numbers of astrosil and graphite inclusions (Voshchinnikov et al. 2005). The curves are computed for an assumed grain number density of $n(r) \propto r^{-3}$.

and graphite inclusions, based on the values of Q_{sca} and g for such grains computed by Voshchinnikov et al. (2005). Figure 20*d* depicts an intermediate case of 60% porosity and pure astrosil derived from values of Q_{sca} and g computed by Wolff et al. (1998). For $x > 25$ we extrapolated the tabulated values of Q_{sca} and g for porous grains to the geometric-optics limits of $Q_{sca} \rightarrow 1$ and $g \rightarrow 1$ as $x \rightarrow \infty$. This extrapolation is acceptable because even the most porous grains are expected to be strongly forward-scattering for $x \gg 25$ (N. Voshchinnikov 2005, private communication) and thus, for $\nu = 3$, contribute negligibly to our edge-on view of the disk.

Figures 20*a* and 20*b* represent the grain characteristics most often invoked when modeling scattered-light images of debris disks. When viewed edge-on, disks comprising compact grains with $a \gg 1$ μm exhibit similar scattering efficiencies in F435W, F606W, and F814W; i.e., they are neutral, albeit relatively inefficient, scatterers at optical wavelengths. This condition is the basis of previous assertions that the reportedly neutral colors of β Pic's disk reflect a minimum grain size of several microns (Paresce & Burrows 1987; Lecavelier des Etangs et al. 1993). However, as noted by Chini et al. (1991), the values of $\langle Q_{eff} \rangle$ for smaller grains ($a \approx 0.2$–0.3 μm) are also similar among the broad

optical bands, so some submicron-sized grains are also neutral scatterers at these wavelengths. Moreover, because small grains likely dominate the size distribution of grains in the disk (Dohnanyi 1969; Li & Greenberg 1998), they more strongly influence the overall color of the disk than supermicron-sized grains. Nevertheless, the truly red colors of β Pic's composite disk (Fig. 18) make the debate over the cause of neutral colors in this case irrelevant.

Figures 20*c*–20*e* show that increasing porosity has two dramatic effects on $\langle Q_{eff} \rangle$. First, the pronounced peak at 0.2–0.4 μm diminishes rapidly for porosities $\gtrsim 60\%$. This phenomenon is caused by the similar behavior of Q_{sca} for $x \lesssim 10$ as porosity increases (Wolff et al. 1998; Voshchinnikov et al. 2005). Second, the peak broadens as it diminishes, causing the ranges of predominantly blue-, neutral-, and red-scattering grains to broaden and shift to larger grain sizes. For 90% porosity, almost all grains with $a \lesssim 3$ μm scatter light in F435W more efficiently than in F606W and F814W, and grains with $a \gtrsim 3$ μm are neutral scatterers. The values of $\langle Q_{eff} \rangle$ for blue-scattering grains with $a \lesssim 1$ μm are less than half those of the neutrally scattering grains, but no distribution of sizes for 90% porous grains will yield a disk with red colors.
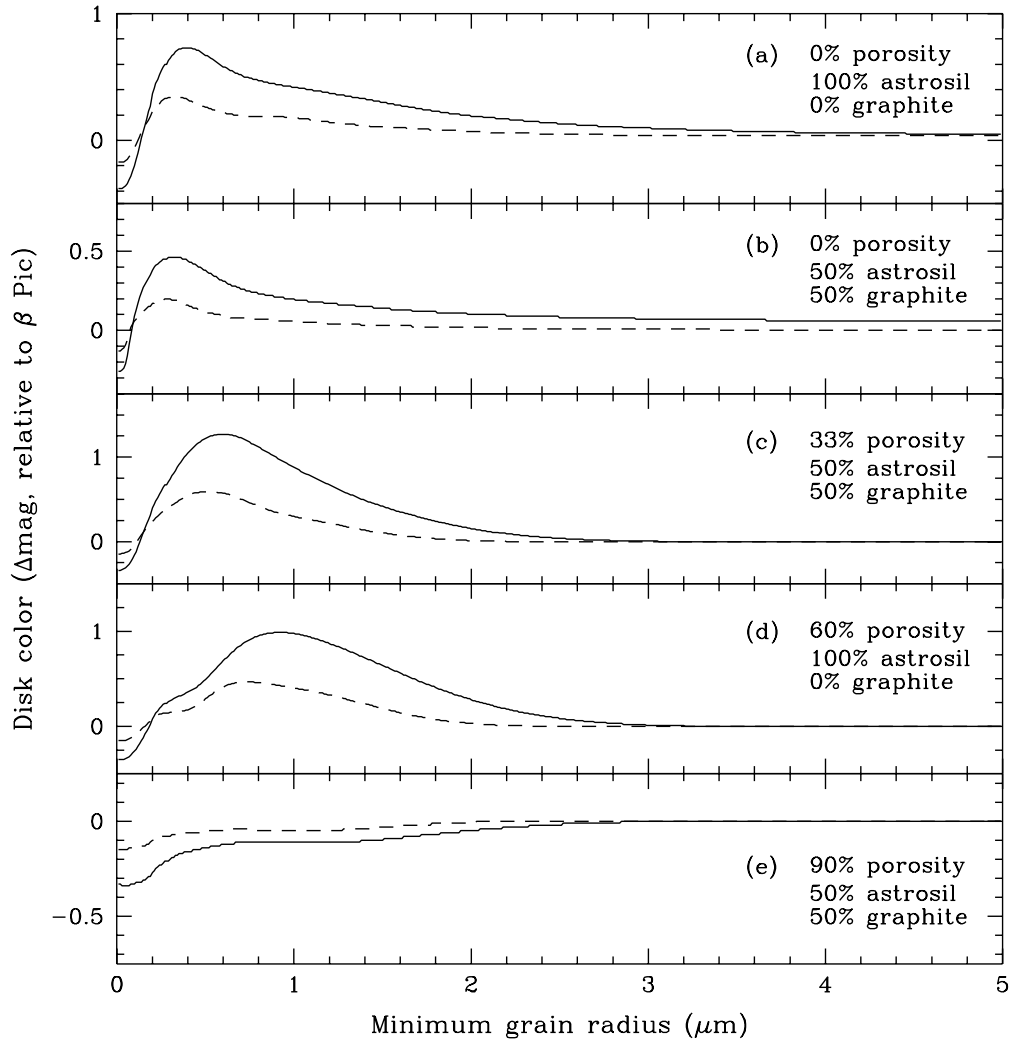
Fig. 21.—Simulated ACS F435W − F606W colors (*dashed curves*) and F435W − F814W colors (*solid curves*) of the disk (relative to those of β Pic) as functions of minimum grain size for various grain compositions and porosities. The colors are derived from the corresponding values of $\langle Q_{\rm eff} \rangle$ shown in Fig. 20 and a grain size distribution of $dn \propto a^{-3.5}\, da$ (Dohnanyi 1969). They pertain to the nonicy grains expected within the ice sublimation zone within ∼100 AU of the star (Pantin et al. 1997; Li & Greenberg 1998). The colors of the composite disk in this region, measured from our PSF-deconvolved images (Fig. 18), are F435W − F606W ≈ 0.1 and F435W − F814W ≈ 0.2.

To compare the colors of an ensemble of grains having uniform porosity and composition with the observed colors of β Pic's disk, we must determine for each bandpass the mean scattering cross section of the ensemble using $\langle Q_{\rm eff} \rangle$ and a reasonable grain size distribution. Applying this quantity to equation (3), we express the intensity of scattered light from the disk relative to the stellar flux in a given bandpass as

$$\mathcal{I} = \frac{I(\epsilon)}{F_*} = \frac{r_0^3}{R^2 \sin^4 \epsilon} \int_{a_{\rm min}}^{a_{\rm max}} \pi a^2 \langle Q_{\rm eff} \rangle \frac{dn_0}{da}\, da, \qquad (9)$$

where $F_* = F_0 r_0^2 / R^2$ is the stellar flux measured at Earth, dn_0/da is the grain size distribution, and $a_{\rm min}$ and $a_{\rm max}$ are the minimum and maximum sizes of the grains. The intrinsic color of the disk between bandpasses 1 and 2 is therefore

$$m_1 - m_2 = -2.5 \log \left(\frac{\mathcal{I}_1}{\mathcal{I}_2} \right). \qquad (10)$$

Figure 21 shows the simulated F435W − F606W and F435W − F814W colors of the inner disk as functions of minimum grain size for the grain compositions and porosities previously con-

sidered. To compute these colors, we assumed the values of $\langle Q_{\rm eff} \rangle$ from Figure 20 and a power-law size distribution, $dn_0 \propto a^{-3.5}\, da$, commonly attributed to dust produced from planetesimal and particle collisions (Dohnanyi 1969). We computed the integral in equation (9) for $a_{\rm min} = 0.01, 0.02, \ldots, 5.00$ μm and an arbitrary $a_{\rm max} = 100$ μm.[26] Except for the case of 90% porosity, the observed colors along the spine of the composite disk within 120 AU (F435W − F606W ≈ 0.1 and F435W − F814W ≈ 0.2; Fig. 18) are simultaneously reproduced by all combinations of porosity and composition when $a_{\rm min} = 0.15$–0.20 μm. The 90% porous grains yield only blue or neutral colors for any choice of $a_{\rm min}$ (as presaged by Fig. 20e) and therefore alone fail to explain the observed red colors of the inner disk.

Our measured colors along the spine of the composite disk within 120 AU are, by themselves, insufficient to constrain tightly the composition and porosity of the grains in that region.

_____

[26] We repeated this exercise for the porous-grain cases using the grain mass distribution derived by Li & Greenberg (1998) from their thermal dust model that assumed 97.5% porosity and $n(r) \propto r^{-1.8}$ within the region 46 AU ≤ r ≤ 115 AU (Fig. 11c of Li & Greenberg 1998). The results were nearly identical to those obtained for the grain size distribution of Dohnanyi (1969), so we discuss them no further.

However, they do show that very porous grains do not contribute significantly to the integrated scattered light along the spine. This conclusion does not necessarily imply a lack of very porous grains, because the values of $\langle Q_{\mathrm{eff}} \rangle$ for such grains with $a \lesssim 2\ \mu m$ are 10–20 times smaller than those of compact and moderately porous grains of similar size (Fig. 20). Thus, our results do not necessarily contradict those of Li & Greenberg (1998), who found that the dust models that best fitted the observed continuum and 10 μm silicate emission from the disk are those that feature extremely porous (>95%) grains. It remains to be seen, however, whether a distribution of grain porosities can simultaneously satisfy the constraints provided by scattered-light and thermal images of the inner disk.

4.2.3. Dust Grains beyond the Ice Sublimation Zone

Our estimate of $a_{\mathrm{min}} = 0.15 - 0.20\ \mu m$ within 120 AU matches that obtained by Voshchinnikov & Krügel (1999) using ground-based observations of the disk's colors and polarization beyond 115 AU (Paresce & Burrows 1987; Lecavelier des Etangs et al. 1993; Wolstencroft et al. 1995), and a dust model featuring an R-band refractive index of $m_R = 1.152 - 0.005i$ and a grain size distribution of $dn \propto a^{-3.2}\ da$. This refractive index is descriptive of both "dirty-ice" grains with 50% porosity and astrosil grains of 76% porosity. However, our HRC images show that the disk steadily reddens beyond 120 AU, so the other dust models considered by Voshchinnikov & Krügel (1999)—and rejected because they produced colors that were too red compared with the nearly neutral colors observed from the ground—are in fact potentially viable models for this region of the disk. These models feature larger refractive indices (corresponding to various combinations of compact and moderately porous grains of astrosil, mixed or layered with dirty ice) and larger a_{min}. In another study of the disk's polarization and colors, Krivova et al. (2000) also favored models with moderate refractive indices, porosities $\lesssim 50\%$, and depleted numbers of grains smaller than $2-3\ \mu m$.

Although tabulated values of Q_{sca} and g have not yet been published for moderately porous astrosil grains with icy mantles, it is reasonable to expect that the optical colors of an edge-on disk of such grains vary with a_{min} in a manner similar to those depicted in Figures 21a–21d. If so, then the increasingly red color gradient observed in β Pic's disk beyond 120 AU (Fig. 18) may reflect values of a_{min} that increase with distance from $\sim 0.15\ \mu m$ to perhaps $\sim 2\ \mu m$ at 250 AU (Voshchinnikov & Krügel 1999). A similar trend was proposed by Weinberger et al. (2003) based on the disappearance of the 10 μm silicate emission feature beyond 20 AU of the star. These phenomena are consistent with the scenario of a diminished presence of small ($a \lesssim 2-3\ \mu m$) grains near the ice sublimation zone ($\gtrsim 100$ AU), where cometary activity ceases (Li & Greenberg 1998) and radiation pressure sets a_{min} to 1–10 μm, depending on porosity (Artymowicz 1988). The steeper color gradients in the southwest extension of the disk suggest that a_{min} increases more rapidly in that extension, i.e., the number of small grains in the southwest extension is smaller than in the northeast extension. This suggestion is consistent with the observed asymmetry between the polarizations of the two extensions (Wolstencroft et al. 1995), which has been attributed to a 20%–30% larger population of small grains in the northeast extension (Krivova et al. 2000).

4.2.4. Dust Grains in the Secondary Disk

The largely uncertain colors of the secondary disk (§ 3.3.3) prevent us from rigorously comparing the grain characteristics of the main and secondary disks. However, the lack of inflec-

tions in the secondary disk's color and surface brightness profiles (Fig. 16) indicates that the grain populations of the two component disks are fundamentally different at 80–150 AU from the star. If the inflections in the main disk's profiles at ~ 115 AU are solely caused by ice sublimation, then the composition and/or size distribution of the secondary disk's grains must be sufficiently different from those of the main disk that the ice sublimation boundary in the secondary disk (if it exists) lies within or beyond the 80–150 AU range of our analysis. More precise photometry of the secondary disk is needed to determine whether the differences in the grains' composition or size distribution required for such a boundary shift are compatible with the colors of the disk.

Artymowicz (1997) argued that icy grains should not exist anywhere in β Pic's disk because they quickly photoevaporate in the face of the star's strong ultraviolet flux and because they are structurally brittle and unable to survive high-velocity collisions with other grains. If so, then other causes of the differences between the color and surface brightness profiles of the main and secondary disks must be considered. For example, the inflections in the main disk's profiles at ~ 115 AU may reflect a sharp decrease in the number density of grains within that distance from the star. Lecavelier des Etangs et al. (1996) successfully modeled the inflection in the surface brightness profile by imposing a lower limit on the sizes of comets or asteroids that travel from outer regions of the disk and retain enough volatile material to evaporate within 110 AU. If this scenario is correct, then the lack of inflections in the secondary disk's profiles suggests that most of its dust is produced by colliding or evaporating planetesimals orbiting near the star rather than by evaporating comets with large, eccentric orbits. This interpretation is consistent with the hypothesis that the "warp" in the composite disk is caused by radiation-blown dust from colliding planetesimals that have been perturbed from the innermost part of the main disk by a giant planet in an inclined orbit (Mouillet et al. 1997b; Augereau et al. 2001).

4.2.5. Possible Effect of Irradiation on Disk Colors

Recent photometric studies of Kuiper Belt objects (KBOs) reveal that these objects exhibit a broad range of optical and near-infrared colors (Luu & Jewitt 1996; Jewitt & Luu 1998, 2001; Tegler & Romanishin 1998, 2003; Barucci et al. 2001; Delsanti et al. 2004). Growing (but controversial) evidence suggests that KBOs are divided by their perihelia, q, into two color populations: KBOs with $q < 40$ AU have neutral-to-red intrinsic colors, and KBOs with $q > 40$ AU have only red intrinsic colors ($0.5 \lesssim B - R \lesssim 0.75$, relative to the Sun; Tegler & Romanishin 1998, 2003; Delsanti et al. 2004). A possible cause of this color trend is the diminution of collisions and/or cometary activity in the outer Kuiper Belt (Luu & Jewitt 1996; Stern 2002; Delsanti et al. 2004). This hypothesis rests on the notion that the dirty-ice surfaces of KBOs are progressively polymerized and reddened by high-energy solar and cosmic radiation unless they are recoated with primordial dust ejected by collisions between KBOs or the sublimation of H_2O, CO_2, and CO ices.

The observed reddening of β Pic's disk beyond its ice sublimation zone suggests a possible connection with the reddening of distant KBOs. Could the reddening of β Pic's disk beyond ~ 115 AU be the result of irradiative polymerization rather than an increasing minimum grain size? Luu & Jewitt (1996) simulated the rate of irradiative reddening of KBOs using an inverse exponential function with an e-folding time of $\sim 10^8$ yr. Because the radiation is overwhelmingly solar within the heliopause (Gil-Hutton 2002), we crudely apply this function to the region

of β Pic's disk in our FOV by assuming that the *e*-folding time scales with luminosity and the distance from the star. In this situation the $B - V$ color of long-lived icy grains orbiting β Pic ($L = 8.7\,L_{\odot}$; Crifo et al. 1997) would increase by ∼0.3 mag in a few times 10^8 yr. The lifetimes of grains not quickly expelled from the disk by radiation pressure are limited by either Poynting-Robertson drag or intergrain collisions, depending on their size and location within the disk. At 120–250 AU the minimum lifetimes of grains larger than ∼0.2 μm are constrained by collisions to ∼0.2–2 Myr (Backman & Paresce 1993). Thus, the lifetimes of the grains observed in our HRC images are much too short for the observed color gradient to be caused by irradiative reddening. This condition likely persists throughout the outer disk, because the grain lifetimes beyond ∼500 AU (which are limited by Poynting-Robertson drag) are ∼1% of the irradiative *e*-folding times at those distances.

4.2.6. *Comparing the Disks around β Pic and AU Mic*

The disk around the M dwarf AU Mic, whose spatial velocity and age are similar to those of β Pic (Barrado y Navascués et al. 1999), is the only known debris disk exhibiting blue colors at optical wavelengths (Krist et al. 2005a). Moreover, the disk's F435W − F814W color becomes bluer with increasing distance from the star. The disk extends at least 210 AU from the star and is viewed almost edge-on (Kalas et al. 2004), so the predicted F435W − F814W colors shown in Figure 21 can be compared to the observed ACS colors of the disk if the grains are not icy. In this case the measured F435W − F814W = −0.3 at 30 AU (Krist et al. 2005a) from AU Mic suggests that the disk may be composed of astrosil and/or graphite grains with $a_{\min} < 0.1\ \mu$m for porosities ≲60% or $a_{\min} \approx 0.2\ \mu$m for 90% porosity. The possibility that AU Mic's disk contains smaller or more porous grains than are evident in β Pic's inner disk (§ 4.2.2) is consistent with the much lower radiation pressure exerted on such grains by AU Mic than by β Pic (Kalas et al. 2004; Krist et al. 2005a). On the other hand, the measured F435W − F814W = −0.5 at 60 AU from the star cannot be produced by any combination of grain composition and porosity shown in Figure 21, so the grains in AU Mic's disk may have a different mineral composition altogether.

5. SUMMARY AND CONCLUDING REMARKS

We have presented *B*-, broad *V*-, and broad *I*-band coronagraphic images of the dusty debris disk around β Pictoris obtained with the High Resolution Channel of *HST*'s Advanced Camera for Surveys. We have exploited the HRC's image resolution and stability by subtracting a well-matched coronagraphic reference image and deconvolving the instrumental PSF from the multiband images. The resulting images provide the most morphologically detailed and photometrically accurate views of the disk between 30 and 300 AU from the star obtained to date.

Our PSF-deconvolved images confirm that the apparent warp in the disk ≲100 AU from the star, which was previously observed by Burrows et al. (1995) and Heap et al. (2000) and modeled by Mouillet et al. (1997b) and Augereau et al. (2001), is a distinct secondary disk inclined to the main disk by ∼5°. The opposing extensions of the secondary disk are not collinear, but their outwardly projected midplanes (spines) are coincident with the isophotal inflections previously seen at large distances and commonly called the "butterfly asymmetry" (Kalas & Jewitt 1995). The surface brightness profiles along the spines of the secondary disk from 80 to 150 AU can be fitted with single power-law functions having indices of $-3.7 < -\alpha < -5.0$. The lack of inflections in the surface brightness profiles around the

expected ice sublimation boundary (∼100 AU) suggests that the composition and/or size distribution of grains in the secondary disk are different from those of the main disk. Altogether, these phenomena support the notion that the secondary disk and the butterfly asymmetry comprise radiatively expelled dust from colliding planetesimals in inclined orbits near the star rather than from evaporating comets in large, eccentric orbits.

We confirm the "wing-tilt asymmetry" between the opposing extensions of the main disk, but we find that the effect is centered on the star rather than offset toward the southwest extension (Kalas & Jewitt 1995). While the spine of the northeast extension appears linear 80–250 AU from the star, the southwest spine is distinctly bowed, with an amplitude of ∼1 AU. The vertical width of the main disk within ∼120 AU is nearly constant and is up to 50% narrower than previously reported. The clumpy structures observed in mid-infrared images and spectra of the disk (Wahhaj et al. 2003; Weinberger et al. 2003; Okamoto et al. 2004; Telesco et al. 2005) are not seen in our optical scattered-light images. The surface brightness profiles along the spines of the main disk's extensions can be fitted with four distinct power laws separated by inflections at ∼70, 117, and 193 AU. The power-law indices, α, match those of Heap et al. (2000) well within 70 AU of β Pic but are 10%–15% smaller than those of Heap et al. (2000) at 127–193 AU. This discrepancy cannot be attributed to differences in the instrumental PSFs. The indices within 150 AU change significantly after removing the contribution from the secondary disk, so the superposed effects of both disks must be considered in future models of β Pic's circumstellar dust distribution.

The two-dimensional F606W/F435W and F814W/F435W flux ratios of the composite disk are nonuniform and asymmetric about the projected major and minor axes of the disk. Within 150 AU of β Pic, the ratios on the southeast side of the disk are ∼1.0–1.1 times those of the star, while those on the northwest side are ∼1.2–1.4 times those of the star. The redder appearance of the nearer northwest side of the disk is inconsistent with the expectation that forward scattering from disk grains should diminish with increasing wavelength. The F435W − F606W and F435W − F814W colors along the spine of the disk are ∼0.1 and ∼0.2 mag redder, respectively, than those of β Pic at ∼40–120 AU from the star. These color excesses increase steadily beyond ∼120 AU, respectively reaching ∼0.2–0.35 and ∼0.25–0.4 mag at 250 AU. These results contradict the long-standing notion that the disk consists of neutrally scattering grains with sizes larger than several microns (Paresce & Burrows 1987; Lecavelier des Etangs et al. 1993).

We have compared the colors measured along the spine of the composite disk with those expected for nonicy grains having a number density $\propto r^{-3}$ and different compositions, porosities, and minimum grain sizes. We find that the observed F435W − F606W and F435W − F814W colors within the ice sublimation zone (≲100 AU) are consistent with those of compact or moderately porous ($P \lesssim 60\%$) grains of astronomical silicate and/or graphite with minimum sizes of ∼0.15–0.20 μm. The observed colors are inconsistent with the blue colors expected from the very porous grains ($P \gtrsim 90\%$) that best reproduce the 10 μm silicate emission feature observed within ∼35 AU of the star (Li & Greenberg 1998). The reddening colors beyond ∼120 AU may reflect the formation of dirty-ice grains or an increasing minimum grain size beyond the ice sublimation boundary. The latter condition is consistent with the decreased production of submicron grains as cometary activity diminishes. It is unlikely that the reddening of the disk beyond ∼120 AU is caused by

irradiative polymerization (as has been postulated for the reddest and most distant Kuiper Belt objects) because the required irradiation time is hundreds of times longer than the expected lifetimes of the grains at those distances.

Our ACS/HRC coronagraphic images of β Pic's disk are the finest multiband, scattered-light images of its inner region (30–300 AU) ever recorded. These images will not be superseded by the *Terrestrial Planet Finder* or other proposed extrasolar-planet imaging missions because the fields of view of those missions will lie well within the region obscured by the HRC's occulting spot. Comparable infrared images of the disk are expected from the *James Webb Space Telescope* if the current specifications for its coronagraphic-imaging modes are maintained. Thus, our observations and derived results should be standard references for comparative and theoretical studies of circumstellar debris disks for at least the next decade.

REFERENCES

Aitken, D. K., Moore, T. J. T., Roche, P. F., Smith, C. H., & Wright, C. M. 1993, MNRAS, 265, L41

Ardila, D. R., et al. 2004, ApJ, 617, L147

———. 2005, ApJ, 624, L141

Artymowicz, P. 1988, ApJ, 335, L79

———. 1997, Ann. Rev. Earth Planet Sci., 25, 175

Artymowicz, P., Burrows, C. J., & Paresce, F. 1989, ApJ, 337, 494

Artymowicz, P., Paresce, F., & Burrows, C. J. 1990, Adv. Space Res., 10 (3), 81

Augereau, J. C., Nelson, R. P., Lagrange, A. M., Papaloizou, J. C. B., & Mouillet, D. 2001, A&A, 370, 447

Aumann, H. H. 1985, PASP, 97, 885

Backman, D. E., & Paresce, F. 1993, in Protostars and Planets III, ed. E. H. Levy & J. I. Lunine (Tucson: Univ. Arizona Press), 1253

Barrado y Navascués, D., Stauffer, J. R., Song, I., & Caillault, J.-P. 1999, ApJ, 520, L123

Barucci, M. A., Fulchignoni, M., Birlan, M., Doressoundiram, A., Romon, J., & Boehnhardt, H. 2001, A&A, 371, 1150

Bessel, M. S. 1990, A&AS, 83, 357

Beust, H., Lagrange-Henri, A. M., Vidal-Madjar, A., & Ferlet, R. 1990, A&A, 236, 202

Beust, H., & Morbidelli, A. 1996, Icarus, 120, 358

Buitrago, J., & Mediavilla, E. 1986, A&A, 162, 95

Burrows, C. J., et al. 1995, BAAS, 27, 1329

Bushouse, H., et al. 1998, Synphot User's Guide (Baltimore: STScI)

Chini, R., Krügel, E., Shustov, B., Tutukov, A., & Kreysa, E. 1991, A&A, 252, 220

Clampin, M., et al. 2003, AJ, 126, 385

Crifo, F., Vidal-Madjar, A., Lallement, R., Ferlet, R., & Gerbaldi, M. 1997, A&A, 320, L29

Delsanti, A., Hainaut, O., Jourdeuil, E., Meech, K. J., Boehnhardt, H., & Barrera, L. 2004, A&A, 417, 1145

Dohnanyi, J. W. 1969, J. Geophys. Res., 74, 2531

Draine, B. T., & Lee, H. M. 1984, ApJ, 285, 89

Ford, H. C., et al. 2003, Proc. SPIE, 4854, 81

Gil-Hutton, R. 2002, Planet. Space Sci., 50, 57

Gledhill, T. M., Scarrott, S. M., & Wolstencroft, R. D. 1991, MNRAS, 252, 50P

Golimowski, D. A., Durrance, S. T., & Clampin, M. 1993, ApJ, 411, L41

Gonzaga, S., et al. 2005, ACS Instrument Handbook, Ver. 6.0 (Baltimore: STScI)

Grady, C. A., et al. 2003, PASP, 115, 1036

Gunn, J. E., & Stryker, L. L. 1983, ApJS, 52, 121

Heap, S. R., Lindler, D. J., Lanz, T. M., Cornett, R. H., Hubeny, I., Maran, S. P., & Woodgate, B. 2000, ApJ, 539, 435

Henyey, L. G., & Greenstein, J. L. 1941, ApJ, 93, 70

Jewitt, D. C., & Luu, J. X. 1998, AJ, 115, 1667

———. 2001, AJ, 122, 2099

Kalas, P., Deltorn, J.-M., & Larwood, J. 2001, ApJ, 553, 410

Kalas, P., & Jewitt, D. 1995, AJ, 110, 794

Kalas, P., Larwood, J., Smith, B. A., & Schultz, A. 2000, ApJ, 530, L133

Kalas, P., Liu, M. C., & Matthews, B. C. 2004, Science, 303, 1990

Knacke, R. F., Fajardo-Acosta, S. B., Telesco, C. M., Hackwell, J. A., Lynch, D. K., & Russell, R. W. 1993, ApJ, 418, 440

Krist, J. 2000, Instrument Sci. Rep. ACS 2000-004 (Baltimore: STScI)

———. 2002, Instrument Sci. Rep. ACS 2002-011 (Baltimore: STScI)

Krist, J., & Hook, R. 2004, The Tiny Tim User's Guide, Ver. 6.3 (Baltimore: STScI)

Krist, J., Mack, J., & Bohlin, R. 2004, Instrument Sci. Rep. ACS 2004-016 (Baltimore: STScI)

Krist, J. E., et al. 2005a, AJ, 129, 1008

———. 2005b, AJ, 130, 2778

Krivova, N. A., Krivov, A. V., & Mann, I. 2000, ApJ, 539, 424

Lagage, P. O., & Pantin, E. 1994, Nature, 369, 628

Lagrange, A.-M., Backman, D. E., & Artymowicz, P. 2000, in Protostars and Planets IV, ed. V. Mannings, A. P. Boss, & S. S. Russell (Tucson: Univ. Arizona Press), 639

Lagrange-Henri, A. M., Vidal-Madjar, A., & Ferlet, R. 1988, A&A, 190, 275

Larwood, J. D., & Kalas, P. G. 2001, MNRAS, 323, 402

Lazzaro, D., Sicardy, B., Roques, F., & Greenberg, R. 1994, Icarus, 108, 59

Lecavelier des Etangs, A., Vidal-Madjar, A., & Ferlet, R. 1996, A&A, 307, 542

Lecavelier des Etangs, A., et al. 1993, A&A, 274, 877

Li, A., & Greenberg, J. M. 1998, A&A, 331, 291

Lucy, L. B. 1974, AJ, 79, 745

Luu, J. X., & Jewitt, D. C. 1996, AJ, 112, 2310

Meurer, G. R., et al. 2002, in 2002 HST Calibration Workshop, ed. S. Arribas, A. Koekemoer, & B. Whitmore (Baltimore: STScI), 65

Mouillet, D., Lagrange, A.-M., Beuzit, J.-L., & Renaud, N. 1997a, A&A, 324, 1083

Mouillet, D., Larwood, J. D., Papaloizou, J. C. B., & Lagrange, A. M. 1997b, MNRAS, 292, 896

Nakano, T. 1988, MNRAS, 230, 551

———. 1990, ApJ, 355, L43

Okamoto, Y. K., et al. 2004, Nature, 431, 660

Pantin, E., Lagage, P. O., & Artymowicz, P. 1997, A&A, 327, 1123

Paresce, F., & Burrows, C. 1987, ApJ, 319, L23

Pavlovsky, C., et al. 2005, ACS Data Handbook, Ver. 4.0 (Baltimore: STScI)

Press, W. H., Teukolsky, S. A., Vetterling, W. T., & Flannery, B. P. 1992, Numerical Recipes in C: The Art of Scientific Computing (2nd ed.; Cambridge: Cambridge Univ. Press), 683

Richardson, W. H. 1972, J. Opt. Soc. Am., 62, 55

Roques, F., Scholl, H., Sicardy, B., & Smith, B. A. 1994, Icarus, 108, 37

Sirianni, M., et al. 2005, PASP, 117, 1049

Smith, B. A., & Terrile, R. J. 1984, Science, 226, 1421

Stern, S. A. 2002, AJ, 124, 2297

Tegler, S. C., & Romanishin, W. 1998, Nature, 392, 49

———. 2003, Icarus, 161, 181

Telesco, C. M., & Knacke, R. F. 1991, ApJ, 372, L29

Telesco, C. M., et al. 2005, Nature, 433, 133

Thébault, P., Augereau, J. C., & Beust, H. 2003, A&A, 408, 775

Vidal-Madjar, A., et al. 1994, A&A, 290, 245

Voshchinnikov, N. V., Il'in, V. B., & Henning, T. 2005, A&A, 429, 371

Voshchinnikov, N. V., & Krügel, E. 1999, A&A, 352, 508

Wahhaj, Z., Koerner, D. W., Ressler, M. E., Werner, M. W., Backman, D. E., & Sargent, A. I. 2003, ApJ, 584, L27

Weinberger, A. J., Becklin, E. E., & Zuckerman, B. 2003, ApJ, 584, L33

Wolff, M. J., Clayton, G. C., & Gibson, S. J. 1998, ApJ, 503, 815

Wolstencroft, R. D., Scarrott, S. M., & Gledhill, T. M. 1995, Ap&SS, 224, 395

Zuckerman, B. 2001, ARA&A, 39, 549

Zuckerman, B., Song, I., Bessell, M. S., & Webb, R. A. 2001, ApJ, 562, L87